

Article

# Efflorescent Sulfate Crystallization on Fractured and Polished Colloform Pyrite Surfaces: A Migration Pathway of Trace Elements

Dimitrina Dimitrova <sup>1,\*</sup> , Vassilka Mladenova <sup>2</sup> and Lutz Hecht <sup>3</sup> <sup>1</sup> Geological Institute, Bulgarian Academy of Sciences, 1113 Sofia, Bulgaria<sup>2</sup> Faculty of Geology and Geography, Sofia University St. Kliment Ohridski, 1504 Sofia, Bulgaria; vassilka@gea.uni-sofia.bg<sup>3</sup> Museum für Naturkunde, Leibniz-Institut für Evolutions und Biodiversitätsforschung, 10115 Berlin, Germany; lutz.hecht@mfn.berlin

\* Correspondence: didi@geology.bas.bg

Received: 5 November 2019; Accepted: 19 December 2019; Published: 21 December 2019



**Abstract:** The colloform pyrite variety incorporates many trace elements that are released in the environment during rapid oxidation. Colloform pyrite from the Chiprovtsi silver–lead deposit in Bulgaria and its oxidation efflorescent products were studied using X-ray diffractometry, scanning electron microscopy, electron microprobe analysis, and laser ablation inductively coupled plasma mass spectrometry. Pyrite is enriched with (in ppm): Co (0.1–964), Ni (1.8–3858), Cu (2.9–3188), Zn (3.1–77), Ag (1.2–1771), As (8179–52,787), Se (2.7–21.7), Sb (48–17792), Hg (4–2854), Tl (1.7–2336), Pb (13–7072), and Au (0.07–2.77). Gypsum, anhydrite, szomolnokite, halotrichite, römerite, copiapite, aluminocopiapite, magnesiocopiapite, coquimbite, aluminocoquimbite, voltaite, and ammoniomagnesiovoltaite were identified in the efflorescent sulfate assemblage. Sulfate minerals contain not only inherited elements from pyrite (Cr, Fe, Co, Ni, Cu, Zn, Ag, In, As, Sb, Hg, Tl, and Pb), but also newly introduced elements (Na, Mg, Al, Si, P, K, Ca, Sc, Ti, V, Mn, Ga, Rb, Sr, Y, Zr, Sn, Cs, Ba, REE, U, and Th). Voltaite group minerals, copiapite, magnesiocopiapite, and römerite incorporate most of the trace elements, especially the most hazardous As, Sb, Hg, and Tl. Colloform pyrite occurrence in the Chiprovtsi deposit is limited. Its association with marbles would further restrict the oxidation and release of hazardous elements into the environment.

**Keywords:** colloform pyrite; oxidation; efflorescent iron sulfates; LA-ICP-MS; trace elements in pyrite and sulfates; Chiprovtsi deposit

## 1. Introduction

Pyrite is the most worldwide abundant sulfide mineral, occurring as a major constituent in ore mineralizations of various types and origin (from magmatic and hydrothermal to sedimentary geologic environments). Pyrite (FeS<sub>2</sub>) incorporates metals, metalloids, and non-metals in the structure through isovalent (Mn<sup>2+</sup>, Co<sup>2+</sup>, Ni<sup>2+</sup>, Cu<sup>2+</sup>, Zn<sup>2+</sup>, Hg<sup>2+</sup>, Pb<sup>2+</sup> for Fe<sup>2+</sup>; Se and Te for S) and heterovalent (Cu<sup>+</sup>, Ag<sup>+</sup>, Au<sup>+</sup>, Bi<sup>+</sup>, Tl<sup>+</sup>, As<sup>3+</sup>, for Fe<sup>2+</sup>; As<sup>−</sup> and Sb<sup>−</sup> for S) substitutions to an extent of percents [1–8]. Recent studies of its trace element geochemistry show trends of element associations in different deposit types [2–8]. This feature determined pyrite as a mineral marker for the evolution of a hydrothermal fluid both in time and space. Pyrite has been proved to be a major carrier of gold where it occurs either as “invisible gold” (nanoparticulate and structurally bound) [9–18] or precipitates within the cracks of earlier As-rich pyrite as microscopically visible gold. It is considered that As content electrochemically facilitates Au deposition in the cracks [1,19]. It is used as a source for the extraction of gold and other

trace metals, such as thallium, and the production of sulfuric acid. However, its abundance makes pyrite also the major constituent of mine waste and the main contributor to the formation of acid mine drainage in some mining areas. The latter being a result of the high reactivity to oxygen and water. Pyrite oxidation [20–24] leads to the formation of a number of water-soluble sulfates [25–30]. Their formation in situ on pyrite-containing wastes in tailing impoundments or other waste storage facilities is more abundant but can be observed during certain environmental conditions, usually employing low humidity.

However, the “colloform”/spherulitic pyrite tends to accommodate more trace elements due to the conditions of its formation (supersaturated fluids and rapid crystal growth [31–37]) and also oxidizes more rapidly to produce efflorescent sulfates due to the larger reactivity area.

The phenomenon of sulfate crystallization on samples containing “colloform”/spherulitic pyrite during their laboratory storage gives a unique opportunity of direct observation of this process, and information to what extent the trace elements incorporated in pyrite can be mobilized into the environment and behave as pollutants.

In this study, we report data on the trace element composition of colloform pyrite from the Ag–Pb Chiprovtsi deposit (NW Bulgaria) and the mineralogy and trace element composition of the efflorescent sulfates formed during its oxidation in laboratory conditions. The results are interpreted with respect to the partitioning of inherited trace elements among newly formed sulfates and their environmental significance.

## 2. Geological Background

The Chiprovtsi silver–lead deposit represents the central and eastern part of an ore zone that extends from the outcropping in NW–W direction Sveti Nikola granite to the E of the Zhelezna village in the Western Balkan Mountains (Bulgaria) (Figure 1). The western part of the ore zone is known as the Martinovo iron skarn deposit. The formation of the ore zone is considered by some researchers [38,39] to be associated with the syntectonic emplacement of the Sveti Nikola granite pluton ( $311.9 \pm 4.1$  Ma, [40]) into the low-metamorphic rocks (marbles and schists) of the so-called diabase–phyllitoid complex (DFC) in Bulgaria during the last Variscan collisional events. Others [41,42] suggest the influence of another undiscovered magmatic source of hydrothermal fluids in depth in addition to the Sveti Nikola pluton. The low-metamorphic rocks of DFC, which form the Paleozoic core of the Alpine Berkovitsa anticline, are a set of ophiolite (Cherni Vrah complex), island-arc (Berkovitsa complex), and continental remnants (Dalgi Del complex) related to the evolution of the Proto-Tethys Ocean (Cambrian–Ordovician age, [43–45]), as the ophiolite part was dated back to be Early Devonian and related to the Southern Variscan suture [46]. The low-metamorphic rocks of Dalgi Del complex occur to the south of the region shown on Figure 1.

The Ag–Pb metasomatic replacement mineralization spatially associates with siderite bodies, which are hosted by thick marble layers in the metamorphic series (Berkovitsa complex) outlined on an area extending 0.5 km north–northwest of the village of Martinovo to the north of the village of Zhelezna. The siderite bodies (>30) occur as mostly concordant layers and lenses, with various thicknesses (10–15 m) and lengths (up to 200 m), with banded, columnar, or tubular shapes. Some of them are bent, boudinaged, and affected by brittle deformations. Transverse right reverse-slip faults with N–NW and N–NE direction break and transpose parts of the marble layers, forming zones of intensive fracturing and brecciation. These zones together with the foliation and brittle deformations in siderite are a favorable environment for the deposition of the hydrothermal ore mineralization [47,48]. The morphology of the ore bodies mostly concurs with the morphology of the siderite bodies. Ore mineralization occurs as veins, veinlets, metasomatic nests, and impregnations within the siderite bodies. The mineral association comprises galena (~90%), pyrite, sphalerite, chalcopyrite, tetrahedrite–tennantite, and other Ag, Pb–Ag sulfosalts. A low-temperature (<250 °C) quartz–barite–fluorite mineralization is deposited in zones of intensive faulting and displacement of the marble layers in the eastern part of the deposit (Velin Dol and Lukina Padina sections of the Chiprovtsi mine; Figure 1), as barite and fluorite

pervasively replace the calcite marbles. This mineralization spatially associates with late polymetallic galena–chalcopyrite–sulfosalt assemblage, where colloform/spherulitic pyrite and cinnabar locally occur as thin veinlets, metasomatic nests, and breccia fillings, with quartz, calcite, ankerite, and fluorite.

The Chiprovtsi mine extracting the Pb–Ag ores from the Chiprovtsi deposit started underground operation in 1951. It was closed in 1999 after producing 4.79 Mt of Pb at 1.84% [49]. The Chiprovtsi mine was also the largest Ag mine in Bulgaria, although public data on the extracted metal and Ag content of the ore is not available. The extraction of fluorite was done for a short period (2010–2016) in the Velin Dol (VD) and Lukina Padina (LP) mine sections, which is located in the easternmost part of the deposit.

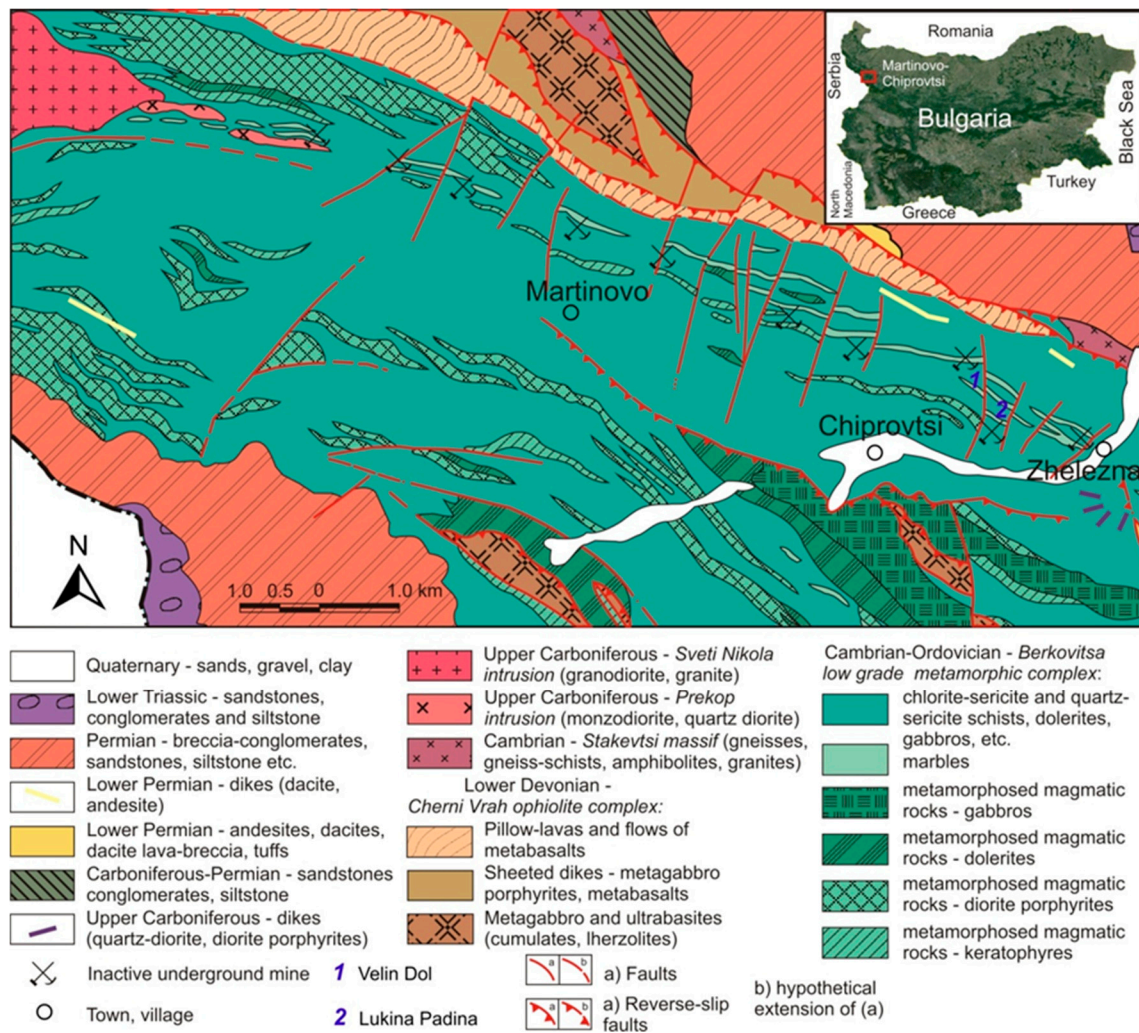


Figure 1. Geological map of the Chiprovtsi ore field, modified after [50].

### 3. Materials and Methods

#### 3.1. Samples

Two types of samples have been studied: (1) aggregates containing abundant colloform pyrite from the low-temperature hydrothermal mineralization occurring in the eastern part of the Chiprovtsi deposit; underground mine workings at level 550 (Velin Dol section) and at levels 495, 606, and 630 (Lukina Padina section) of the mine (Figures 1 and 2); and (2) efflorescent sulfates that have been formed in laboratory conditions on the polished and fractured surfaces of the colloform pyrite containing aggregates from the same deposit. The mineral relationships were studied by reflected light microscopy in polished sections. The chemical composition (major, minor, and trace elements) of colloform pyrite

was determined in four polished sections. The sulfate aggregates were observed on five large (~6–7 cm × 10–12 cm × 20 cm) and four small (2–4 cm × 3–5 cm × 4–5 cm) samples. They were hand-picked under binocular microscope from the surface of the large samples, i.e., not from the part that was cut for polished section preparation. Monomineral sulfate aggregates for LA-ICP-MS analysis were carefully hand-picked at highest magnification (60×) under binocular microscope.

### 3.2. Analytical Procedures

#### 3.2.1. X-Ray Diffractometry (XRD), Scanning Electron Microscopy (SEM), and Electron Microprobe Analysis (EMPA)

A bulk sample of powdered efflorescent aggregates was used for mineral identification by XRD using a PANalytical Empyrean (Institute of Physical Chemistry, Bulgarian Academy of Sciences, Sofia, Bulgaria), equipped with a multichannel detector (Pixel 3D) using (Cu K $\alpha$  45 kV–40 mA) radiation in the 20–115° 2 $\theta$  range, with a scan step of 0.01° for 20 s. The morphology of the newly formed crystal aggregates was examined on gold-coated specimens using a Jeol 5510 SEM (Sofia University, Faculty of Chemistry) in secondary electron operating mode. The chemical composition of sulfates was determined on carbon-coated specimens by a Jeol JXA-8500F microprobe instrument (Museum für Naturkunde, Berlin, Germany). Microprobe analyses of colloform pyrite were performed on a JEOL Superprobe 733, equipped with an ORTEC energy-dispersive system (Geological Institute, Bulgarian Academy of Sciences) at accelerating voltage of the probe 25 keV and using the following standards: pure metals Ag, Ni, Co, Sb<sub>2</sub>S<sub>3</sub> (for Sb), FeS<sub>2</sub> and CuFeS<sub>2</sub> (for Fe), Cu<sub>3</sub>AsS<sub>4</sub> (for Cu, As, and S), ZnS (for Zn), CdS (for Cd), and HgS (for Hg).

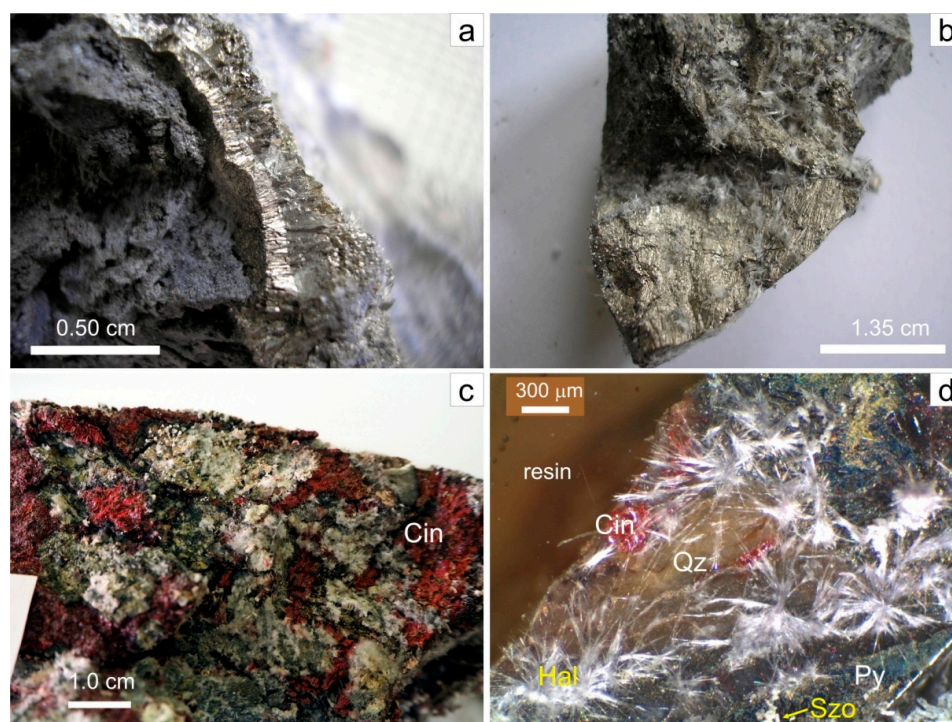


**Figure 2.** Mineral sample aggregates: (a) a fresh silicified rock fragment with coarse radial colloform pyrite from the Velin Dol (VD) mine section, level 550; (b) massive colloform pyrite aggregate with oxidation products formed in laboratory conditions; (c,d) slightly oxidized cinnabar-colloform pyrite (+carbonate, fluorite, and quartz) aggregate: fragment (c) and polished section (d). Samples (b–d) are from the Lukina Padina (LP) mine section, level 495. Image (d) is from a binocular microscope. Abbreviations: Py, pyrite; Cin, cinnabar; Qz, quartz; Szo, szomolnokite; Hal, halotrichite.

### 3.2.2. Laser Ablation Inductively Coupled Plasma Mass Spectrometry (LA-ICP-MS)

Trace element concentrations in pyrite and efflorescent sulfates were measured using a PerkinElmer ELAN DRC-e ICP mass spectrometer combined with a New Wave UP193-FX excimer laser ablation system (Geological Institute, Bulgarian Academy of Sciences, Sofia, Bulgaria). The ablation was done in He medium. The ICP-MS was optimized daily to maximize sensitivity and tune the oxide production rate of ThO/Th to <0.5%. The laser system was operated at: (1) 10 Hz repetition rate; 50  $\mu\text{m}$  spot size, and energy density on pyrite sample and standards 2.5–3.0 J/cm<sup>2</sup>; (2) 4 Hz repetition rate; 35  $\mu\text{m}$  spot size, and energy density on sulfate samples and standards 2.5–2.8 J/cm<sup>2</sup>. The analysis time was 100 s, comprising a 40-s measurement of background and a 60-s analysis with a laser-on the sample. The acquisition dwell time for all masses was set to 0.01 s. The following isotopes were monitored in pyrite: <sup>49</sup>Ti, <sup>51</sup>V, <sup>53</sup>Cr, <sup>55</sup>Mn, <sup>57</sup>Fe, <sup>59</sup>Co, <sup>60</sup>Ni, <sup>65</sup>Cu, <sup>66</sup>Zn, <sup>71</sup>Ga, <sup>73</sup>Ge, <sup>75</sup>As, <sup>77</sup>Se, <sup>95</sup>Mo, <sup>107</sup>Ag, <sup>111</sup>Cd, <sup>115</sup>In, <sup>118</sup>Sn, <sup>121</sup>Sb, <sup>125</sup>Te, <sup>182</sup>W, <sup>197</sup>Au, <sup>202</sup>Hg, <sup>205</sup>Tl, <sup>208</sup>Pb, and <sup>209</sup>Bi; with the addition of <sup>23</sup>Na, <sup>25</sup>Mg, <sup>27</sup>Al, <sup>29</sup>Si, <sup>31</sup>P, <sup>39</sup>K, <sup>42</sup>Ca, <sup>45</sup>Sc, <sup>85</sup>Rb, <sup>88</sup>Sr, <sup>89</sup>Y, <sup>90</sup>Zr, <sup>133</sup>Cs, <sup>137</sup>Ba, <sup>139</sup>La, <sup>140</sup>Ce, <sup>146</sup>Nd, <sup>147</sup>Sm, <sup>151</sup>Eu, <sup>232</sup>Th, and <sup>238</sup>U, monitored in sulfates. Analyses were performed on predefined areas of the polished pyrite-containing samples to avoid mineral inclusions. External standardization was done using NIST SRM 610 glass and MASS1 [51] sulfide standards, which were analyzed recurrently throughout the experiment. Data reduction was done using Fe as an internal standard and the SILLS software [52]. The unexpected peak-shaped fluctuations of the intensity signal of some isotopes were avoided during data reduction to exclude the influence of other minerals on the chemical composition of both pyrite and sulfates.

## 4. Results

### 4.1. Colloform Pyrite

#### 4.1.1. Colloform Pyrite Morphology and Mineral Assemblage

Colloform/spherulitic pyrite occurs together with other morphological varieties of pyrite in this low-temperature mineralization: (1) large, fractured grains, with carbonates in veins crosscutting the fluorite bodies; and (2) small euhedral crystals in cinnabar or as inclusions in transparent quartz crystals (Figure 3a). Fine-radial colloform pyrite forms breccia fillings and nests 0.05–15-cm thick with cinnabar, metacinnabar, and quartz (Figure 3a,b), or metasomatically replaces siderite, ankerite, ferrodolomite, and calcite (Figure 3a,c). Relatively coarse radial spherulites overgrow silicified marble. Pyrite is often observed together with other minerals from the late polymetallic assemblage (galena, chalcopyrite, tetrahedrite–tennantite) (Figure 3d), but rarely with marcasite (Figure 3c).

An SEM study of colloform pyrite spherulites associating with cinnabar reveals that the outer surface of the spherulite is not smooth, but consists of numerous pyritohedron crystals with sizes up to 50–60  $\mu\text{m}$  (Figure 3b). Transverse sections of spherulites (Figures 3b and 4) show that they are composed of radial-divergent elongated needle-like crystals along the [001] crystallographic axis of pyrite, which start growing from single or multiple crystal nuclei located on the mineral surface (quartz, calcite), as well as metasomatically replace carbonate medium (Figure 3c). The growth zone width varies from micrometers to 200–300  $\mu\text{m}$  (outer zone). The semi-concentric to concentric zonal banding is determined mostly by differences in chemical composition, the presence of discrete mineral inclusions enveloped by pyrite during crystal growth (tetrahedrite–tennantite, quartz; Figure 4), or interstitial pore space infillings of other minerals (cinnabar, barite, and native silver) (Figures 3b and 4).

These interstitial pore spaces significantly increase the surface of pyrite aggregates, which is exposed to air. Immediate oxidation reactions occur on the pyrite surface when exposed to water or air.

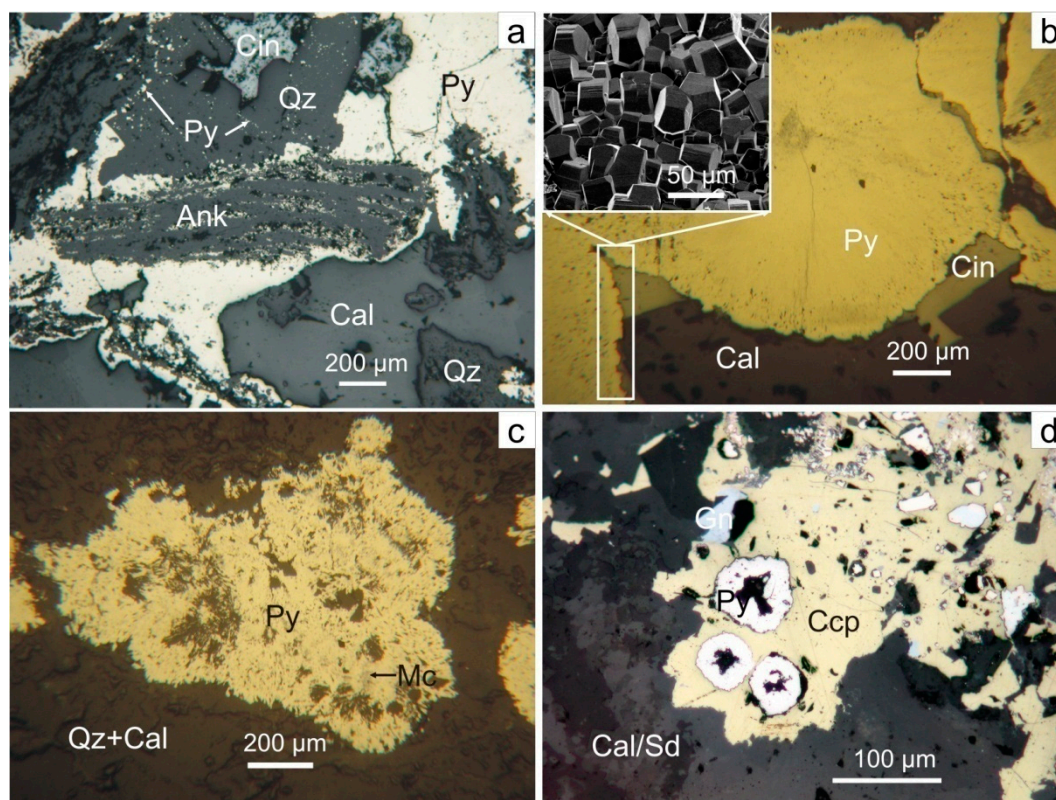


**Figure 3.** Photomicrographs (reflected light) of: (a) pyrite replacing ankerite with cinnabar; (b) a cross-section of pyrite spherulite associated with cinnabar in calcite. SEM image of spherulite surface. The sample is from the Lukina Padina section, level 606; (c) colloform pyrite–marcasite aggregate in silicified carbonate; (d) pyrite spherulites in chalcopyrite and galena; (a,c–d) are from the Lukina Padina section, level 495. Abbreviations: Py, pyrite; Cin, cinnabar; Ccp, chalcopyrite; Gn, galena; Cal, calcite; Ank, ankerite; Sd, siderite; Qz, quartz.

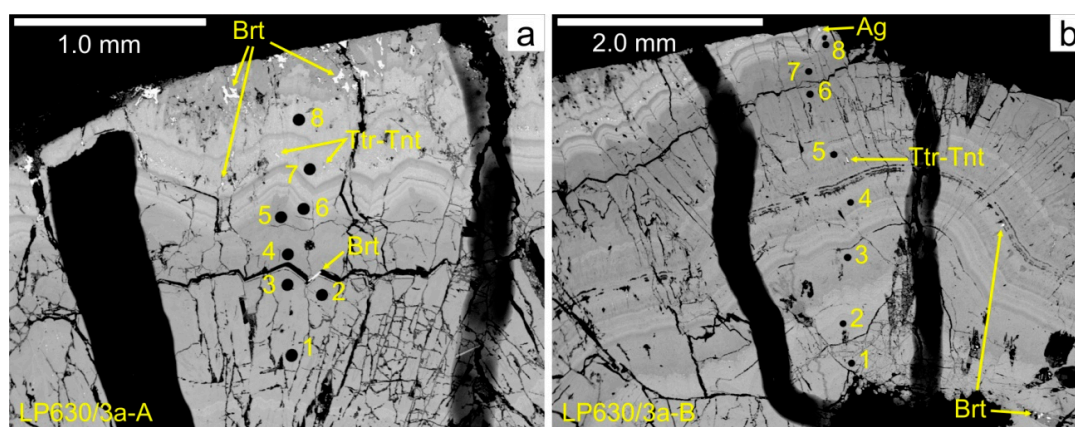


**Figure 4.** SEM back-scattered electron images of colloform pyrite and spots of laser ablation inductively coupled plasma mass spectrometry (LA-ICP-MS) analyses in sample LP630/3a: (a) area A; (b) area B. Numbers of spot analyses are the same as in Tables 1 and 2. Abbreviations: Brt, barite; Ttr-Tnt, tetrahedrite–tennantite; Ag, native silver.

#### 4.1.2. Chemical Composition of Colloform Pyrite

Microprobe analyses show that colloform pyrite contains Cu (up to 0.75 wt.%), Ni (0.01–0.36 wt.%), As (0.74–4.78 wt.%), Sb (up to 2.43 wt.%), and negligible content Ag (<0.15 wt.%) (Table 1). LA-ICP-MS

spot analyses reveal the presence of other trace elements, such as Cr, Mn, Co, Zn, Se, Cd, In, Te, Au, Hg, Tl, Pb, and Bi (Table 2).

A number of trace elements were detected in colloform pyrite by LA-ICP-MS. All intensities of trace element isotopes in time-resolved down-hole ablation profiles were thoroughly examined during data reduction and sudden peak-shaped fluctuations, denoting mineral inclusions and gangue mineral crosscuttings, were avoided/excluded. Flat profiles, featuring a gradual decrease or increase of isotope intensities, were presumed to be a result of stable content of the element in one zone or smooth transition into another adjacent growth zone. However, the ablation of a volume containing a dense cluster of nanoparticulate mineral phases within a host mineral would produce also a subtle flat intensity profile. Thus, the interpretation of the LA-ICP-MS results requires caution.

**Table 1.** Chemical composition of pyrite determined by EMPA, element content in wt.%. An.#, Analysis number.

Sample An.#	Fe	Ni	Cu	Ag	As	Sb	S	Sum	Chemical Formulae
VD1-A p.1	44.16	0.02	0.05	bdl	3.20	1.44	51.42	100.29	Fe <sub>0.97</sub> As <sub>0.05</sub> Sb <sub>0.01</sub> S <sub>1.96</sub>
VD1-A p.3	45.73	0.01	bdl	0.02	1.81	0.44	52.50	100.51	Fe <sub>0.99</sub> As <sub>0.03</sub> S <sub>1.98</sub>
VD1-A p.5	44.17	bdl	0.06	bdl	3.14	1.51	51.27	100.15	Fe <sub>0.97</sub> As <sub>0.05</sub> Sb <sub>0.02</sub> S <sub>1.96</sub>
VD1-A p.7	44.30	0.01	0.01	bdl	3.36	1.44	51.30	100.42	Fe <sub>0.97</sub> As <sub>0.05</sub> Sb <sub>0.01</sub> S <sub>1.96</sub>
VD1-A p.10	44.59	bdl	bdl	bdl	3.05	1.38	51.40	100.48	Fe <sub>0.98</sub> As <sub>0.05</sub> Sb <sub>0.01</sub> S <sub>1.96</sub>
VD1-A p.12	44.59	bdl	0.01	bdl	3.77	1.28	50.44	100.09	Fe <sub>0.98</sub> As <sub>0.06</sub> Sb <sub>0.01</sub> S <sub>1.94</sub>
VD1-B p.1	45.03	0.03	0.03	0.14	3.42	0.96	49.90	99.51	Fe <sub>1.00</sub> As <sub>0.06</sub> Sb <sub>0.01</sub> S <sub>1.93</sub>
VD1-B p.2	43.45	bdl	0.07	bdl	3.63	2.43	50.94	100.52	Fe <sub>0.96</sub> As <sub>0.06</sub> Sb <sub>0.02</sub> S <sub>1.96</sub>
VD1-B p.3	46.03	0.01	bdl	bdl	1.55	0.23	52.92	100.74	Fe <sub>0.99</sub> As <sub>0.02</sub> S <sub>1.98</sub>
VD1-B p.4	44.77	bdl	0.04	0.02	2.75	1.18	51.88	100.64	Fe <sub>0.97</sub> As <sub>0.04</sub> Sb <sub>0.01</sub> S <sub>1.97</sub>
VD1-B p.5	45.54	bdl	0.01	bdl	1.70	0.65	52.37	100.27	Fe <sub>0.99</sub> As <sub>0.03</sub> Sb <sub>0.01</sub> S <sub>1.98</sub>
VD1-B p.6	45.82	bdl	0.05	bdl	1.56	0.33	52.27	100.03	Fe <sub>0.99</sub> As <sub>0.03</sub> S <sub>1.98</sub>
VD2-A p.10	46.35	bdl	bdl	bdl	0.90	0.09	52.74	100.08	Fe <sub>1.00</sub> As <sub>0.01</sub> S <sub>1.99</sub>
VD2-A p.12	46.35	bdl	0.05	bdl	1.07	bdl	52.19	99.66	Fe <sub>1.01</sub> As <sub>0.02</sub> S <sub>1.97</sub>
VD2-A p.4	46.31	bdl	0.04	0.08	1.07	0.12	52.27	99.89	Fe <sub>1.00</sub> As <sub>0.02</sub> S <sub>1.98</sub>
VD2-A p.1	46.40	0.01	0.02	bdl	1.21	0.05	52.26	99.95	Fe <sub>1.01</sub> As <sub>0.02</sub> S <sub>1.97</sub>
VD2-A p.2	46.39	bdl	0.03	0.01	1.22	0.16	52.94	100.75	Fe <sub>1.00</sub> As <sub>0.02</sub> S <sub>1.98</sub>
VD2-B p.1	46.14	0.02	0.07	0.1	1.21	0.43	52.38	100.35	Fe <sub>1.00</sub> As <sub>0.02</sub> S <sub>1.98</sub>
VD2-B p.2	46.34	bdl	0.07	0.12	1.03	0.12	52.86	100.54	Fe <sub>1.00</sub> As <sub>0.02</sub> S <sub>1.98</sub>
VD2-B p.4	46.45	bdl	bdl	bdl	1.29	0.29	52.84	100.87	Fe <sub>1.00</sub> As <sub>0.02</sub> S <sub>1.98</sub>
VD2-B p.6	46.80	bdl	0.07	0.05	1.00	0.15	52.70	100.77	Fe <sub>1.01</sub> As <sub>0.02</sub> S <sub>1.97</sub>
ch603 p.1	45.24	0.19	0.15	bdl	1.40	0.23	51.81	99.02	Fe <sub>0.99</sub> As <sub>0.02</sub> S <sub>1.97</sub>
ch603 p.7	45.51	0.34	0.14	bdl	2.16	0.14	51.11	99.40	Fe <sub>0.99</sub> Ni <sub>0.01</sub> As <sub>0.04</sub> S <sub>1.96</sub>
ch603 p.8	45.47	0.35	0.30	bdl	2.10	0.17	51.27	99.66	Fe <sub>0.99</sub> Ni <sub>0.01</sub> Cu <sub>0.01</sub> As <sub>0.03</sub> S <sub>1.96</sub>
LP630/3a-A p.1	45.42	0.01	bdl	bdl	3.30	0.08	50.87	99.68	Fe <sub>1.00</sub> As <sub>0.05</sub> S <sub>1.95</sub>
LP630/3a-A p.2	46.12	bdl	0.02	bdl	1.88	0.05	51.65	99.72	Fe <sub>1.01</sub> As <sub>0.03</sub> S <sub>1.96</sub>
LP630/3a-A p.3	46.09	bdl	0.02	bdl	1.95	0.06	51.32	99.44	Fe <sub>1.01</sub> As <sub>0.03</sub> S <sub>1.96</sub>
LP630/3a-A p.4	45.78	bdl	0.07	bdl	1.82	0.07	51.52	99.26	Fe <sub>1.00</sub> As <sub>0.03</sub> S <sub>1.97</sub>
LP630/3a-A p.5	46.00	bdl	0.06	bdl	1.84	0.01	51.63	99.54	Fe <sub>1.00</sub> As <sub>0.03</sub> S <sub>1.97</sub>
LP630/3a-A p.6	42.82	bdl	0.61	0.30	4.64	1.48	49.40	99.25	Fe <sub>0.96</sub> Cu <sub>0.01</sub> As <sub>0.08</sub> Sb <sub>0.02</sub> S <sub>1.93</sub>
LP630/3a-A p.8	43.11	bdl	0.75	0.53	4.61	1.25	48.92	99.17	Fe <sub>0.97</sub> Cu <sub>0.01</sub> As <sub>0.08</sub> Sb <sub>0.01</sub> S <sub>1.92</sub>
LP630/3a-B p.2	42.26	0.05	0.06	0.11	4.24	1.15	51.53	99.52	Fe <sub>0.93</sub> As <sub>0.07</sub> Sb <sub>0.01</sub> S <sub>1.99</sub>
LP630/3a-B p.5	43.45	bdl	0.07	bdl	3.78	0.48	51.26	99.10	Fe <sub>0.96</sub> As <sub>0.06</sub> S <sub>1.98</sub>
LP630/3a-B p.6	46.24	0.01	bdl	bdl	0.74	0.04	52.48	99.42	Fe <sub>1.00</sub> As <sub>0.01</sub> S <sub>1.99</sub>
LP630/3a-B p.7	45.63	bdl	bdl	0.03	3.13	0.1	50.83	99.70	Fe <sub>1.00</sub> As <sub>0.05</sub> S <sub>1.95</sub>
LP630/3a-B p.8	45.14	nd	0.02	nd	3.02	0.03	50.91	99.12	Fe <sub>1.00</sub> As <sub>0.05</sub> S <sub>1.95</sub>

bdl, below detection limit of 0.01 wt.%.

**Table 2.** Trace element concentrations in pyrite determined by LA-ICP-MS (ppm). An.#, Analysis number.

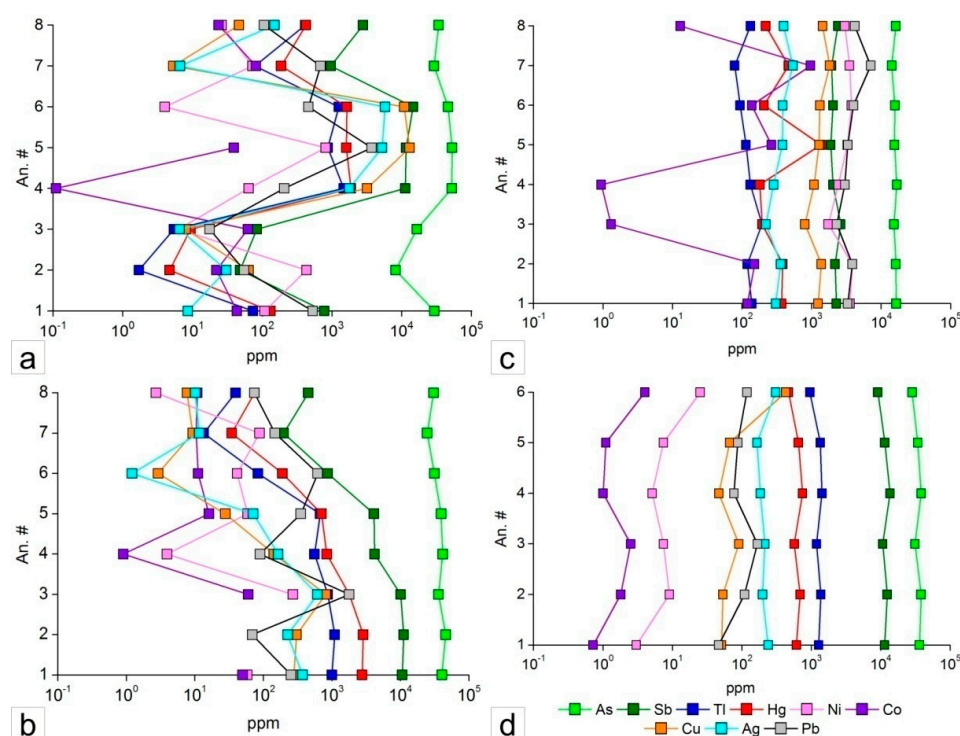
Sample An.#	Cr	Mn	Co	Ni	Cu	Zn	As	Se	Ag	Cd	In	Sb	Te	Au	Hg	Tl	Pb	Bi
VD1-A p.1	4.6	8.4	4.0	25.0	425	8.6	28,225	11.3	305	bdl	bdl	9032	bdl	0.90	467	953	118	bdl
VD1-A p.3	bdl	8.7	1.1	7.4	66.5	12.3	33,863	12.3	165	bdl	bdl	11,371	bdl	1.82	649	1342	87.0	bdl
VD1-A p.5	4.0	8.5	1.0	5.1	46.5	11.1	38,131	21.7	184	bdl	0.02	13,550	bdl	2.45	746	1422	76.7	bdl
VD1-A p.7	5.6	7.9	2.5	7.4	89.8	9.1	30,933	16.0	214	bdl	bdl	10,636	bdl	2.59	567	1186	167	bdl
VD1-A p.10	4.8	8.7	1.8	9.0	53.2	12.2	37,960	13.6	198	0.27	bdl	12,318	bdl	2.77	690	1363	109	bdl
VD1-A p.12	bdl	9.1	0.72	3.0	50.9	12.4	35,970	14.8	239	bdl	0.04	11,302	bdl	1.43	610	1272	46.1	bdl
VD1-B p.1	bdl	7.7	0.10	bdl	117.1	7.8	34,697	7.5	492	bdl	bdl	9442	bdl	0.61	495	1182	13.6	bdl
VD1-B p.2	6.0	7.5	1.0	3.8	229	12.4	35,056	9.4	506	bdl	bdl	16,680	bdl	0.94	1242	2042	47.5	bdl
VD1-B p.3	bdl	6.6	0.10	bdl	1248	7.3	20,033	4.6	1016	bdl	0.03	8673	bdl	0.58	489	782	60.0	bdl
VD1-B p.4	3.9	7.2	0.12	2.0	864	10.7	27,475	bdl	780	bdl	bdl	13,015	bdl	0.53	867	1421	38.8	bdl
VD1-B p.5	bdl	7.9	0.26	bdl	24	14.9	36,788	5.9	85.9	bdl	bdl	17,792	bdl	0.39	1361	2336	13.1	bdl
VD1-B p.6	6.6	7.1	0.90	bdl	225	8.7	30,291	10.2	358	bdl	bdl	11,939	bdl	0.74	760	1304	177	bdl
VD2-A p.10	bdl	7.9	1.4	1.8	127	bdl	10,557	10.3	357	bdl	bdl	1321	bdl	0.53	12.6	45.8	229	bdl
VD2-A p.12	3.9	8.1	1.3	13.0	162	6.4	11,591	bdl	297	1.33	bdl	1103	bdl	0.31	15.9	37.9	418	bdl
VD2-A p.4	2.9	7.1	1.2	bdl	99.3	5.4	10,551	7.4	374	0.26	bdl	1038	bdl	0.42	6.8	34.4	201	bdl
VD2-A p.6	3.3	8.8	0.88	bdl	42.4	6.9	11,341	bdl	159	bdl	bdl	561	bdl	0.36	4.0	25.2	43.0	bdl
VD2-A p.3	3.8	7.4	2.0	5.5	81.7	6.5	10,680	bdl	238	bdl	bdl	809	bdl	0.66	10.8	38.1	118	bdl
VD2-A p.7	6.0	7.7	0.56	bdl	64.4	5.2	10,524	5.2	256	bdl	bdl	726	bdl	0.32	10.6	28.8	69.7	bdl
VD2-A p.1	4.0	7.8	1.17	bdl	64.1	5.5	10,872	5.0	217	bdl	bdl	659	0.86	0.49	5.0	19.1	128	bdl
VD2-A p.2	bdl	7.7	1.0	bdl	77.6	6.0	10,863	5.8	295	0.31	bdl	852	0.98	0.40	7.1	22.7	159	bdl
VD2-B p.1	2.7	7.7	0.92	5.0	156	5.5	11,893	11.0	634	0.55	bdl	1649	0.62	1.28	14.9	84.9	101	bdl
VD2-B p.2	3.9	8.5	0.90	2.1	137	4.8	11,947	13.0	507	0.56	0.02	1436	0.72	1.37	15.2	73.5	93.4	bdl
VD2-B p.3	3.0	7.2	0.85	bdl	139	5.1	11,777	9.1	533	bdl	bdl	1376	0.94	1.18	13.3	73.5	90.2	bdl
VD2-B p.4	bdl	7.1	1.2	3.3	142	6.0	11,818	14.1	570	bdl	0.03	1410	1.16	1.01	14.5	62.6	87.7	bdl
VD2-B p.5	bdl	6.4	0.45	bdl	73.5	3.6	10,360	10.8	296	bdl	bdl	853	bdl	0.76	15.7	57.9	62.5	bdl
VD2-B p.6	3.5	7.7	1.7	4.7	175	7.7	11,242	9.8	690	0.35	bdl	1644	bdl	1.14	12.5	83.5	95.1	bdl
ch603 p.1	20.9	5.9	1.3	1741	799	5.8	15,259	2.7	220	bdl	bdl	2617	bdl	1.19	195	193	2292	0.09
ch603 p.2	4.2	5.2	0.94	2415	1082	4.8	16,809	bdl	283	0.57	0.03	2033	bdl	1.00	180	131	3014	0.13
ch603 p.3	53.6	4.6	265	3280	1281	5.3	15,621	4.7	381	bdl	bdl	1885	bdl	1.43	1359	114	3317	0.09
ch603 p.4	4.6	4.1	138	3724	1314	5.1	15,775	4.1	385	0.54	bdl	2035	bdl	1.71	206	93.7	3986	bdl
ch603 p.5	11.1	5.2	964	3518	1812	4.3	14,183	6.5	536	bdl	0.05	1932	bdl	2.15	467	78.4	7072	0.09
ch603 p.6	4.9	4.7	12.9	2990	1442	4.0	16,252	bdl	394	0.46	bdl	2386	bdl	2.19	218	132	4183	bdl
ch603 p.7	4.5	5.0	119	3549	1244	3.1	16,486	3.8	305	bdl	bdl	2262	bdl	1.90	370	138	3305	0.38
ch603 p.8	4.4	4.7	151	3858	1381	3.9	16,234	5.0	359	0.41	bdl	2172	bdl	1.56	383	119	3840	0.59

Table 2. Cont.

Sample An.#	Cr	Mn	Co	Ni	Cu	Zn	As	Se	Ag	Cd	In	Sb	Te	Au	Hg	Tl	Pb	Bi
LP630/3a-A p.1	47.7	9.5	43.1	108	<8.8	bdl	29,409	5.7	8.6	bdl	bdl	777	bdl	bdl	131	73.8	529	bdl
LP630/3a-A p.2	bdl	5.0	21.9	431	63.7	bdl	8179	bdl	30.6	bdl	bdl	48.2	bdl	bdl	4.7	1.7	55.1	bdl
LP630/3a-A p.3	6.8	5.5	62.3	6.3	8.0	bdl	16,432	bdl	6.5	bdl	bdl	83.3	bdl	bdl	9.4	5.4	17.7	bdl
LP630/3a-A p.4	bdl	5.3	0.11	63.9	3188	48.3	52,322	bdl	1771	8.2	bdl	11,215	0.85	bdl	1874	1467	206	bdl
LP630/3a-A p.5	4.8	7.2	39.1	809	12,971	1152	52,787	bdl	5230	32.3	bdl	11,541	0.72	0.38	1602	871	3702	bdl
LP630/3a-A p.6	bdl	4.9	bdl	4.0	10,798	77.2	46,126	bdl	5746	37.2	bdl	14,527	0.81	0.51	1629	1250	457	bdl
LP630/3a-A p.7	4.6	5.8	80.9	72.5	5.3	4.9	29,101	5.9	6.6	0.32	0.04	957	0.94	bdl	186	78.5	682	bdl
LP630/3a-A p.8	2.3	5.2	23.7	26.2	46.4	4.3	33,788	6.0	150	bdl	0.03	2792	bdl	bdl	425	413	106	bdl
LP630/3a-B p.1	13.3	70.1	49.6	58.0	278	25.3	40,192	3.6	372	0.58	0.02	10,567	bdl	0.07	2752	998	253	bdl
LP630/3a-B p.2	bdl	4.7	bdl	bdl	303	16.3	45,571	3.4	226	0.70	0.02	11,092	1.45	0.15	2854	1095	68.5	bdl
LP630/3a-B p.3	3.0	4.8	60.2	269	808	11.5	35,901	bdl	613	bdl	bdl	10,072	bdl	0.40	1785	864	1783	0.06
LP630/3a-B p.4	2.8	5.0	0.90	3.9	142	14.6	41,365	bdl	164	0.84	0.02	4190	0.63	bdl	840	556	89.3	bdl
LP630/3a-B p.5	3.0	4.7	16.0	58.9	27.8	5.3	39,163	8.1	70.7	1.1	0.02	4096	bdl	0.07	705	672	350	bdl
LP630/3a-B p.6	3.1	5.1	11.1	41.2	2.9	4.1	31,246	5.8	1.21	bdl	0.02	864	1.40	bdl	189	83.0	618	bdl
LP630/3a-B p.7	6.2	6.2	10.4	87.6	9.3	3.7	24,563	bdl	11.6	bdl	bdl	197	0.97	bdl	34.4	13.4	147	bdl
LP630/3a-B p.8	5.1	5.1	10.8	2.7	7.7	bdl	30,402	bdl	10.1	0.22	bdl	451	bdl	bdl	74.3	39.1	73.7	bdl

bdl, below detection limits.

It is seen that Co, Ni, Cu, Ag, As, Sb, Tl, Hg, and Pb are frequent constituents of the colloform pyrite chemistry. Their contents vary in wide range, from tens to thousands of parts per million (ppm), not only on the micronscale (neighboring growth zones) within one spherulite aggregate, but also in ore bodies from Velin Dol and Lukina Padina sections (Figure 5). In some pyrites, the variation range of concentrations in neighboring growth zones is more subtle, in others, it is more distinct, with change even in the element profile. Pyrite from the Lukina Padina section is more enriched in Ni, Co, Hg, and Pb compared to pyrite from the Velin Dol section. The latter one is more enriched in Sb, Tl, Se, and Zn. Arsenic is characteristic for pyrite, with contents usually above 1 wt.%, reaching up to 5.2 wt.%. Although on a different scale, As distribution patterns concur with those of Hg, Tl, and Sb (Figure 5). Arsenic and Sb were also detected everywhere using EMPA, thus suggesting their incorporation in the lattice.



**Figure 5.** Distribution patterns of some trace elements in colloform pyrite growth zones along:(a) and (b) transverse section of sample LP630/3a, areas A and B, respectively; (c,d) randomly orientated sections of colloform pyrite-bearing aggregates in samples ch603 and VD1 (area A), respectively. Samples LP630/3a and ch603 are from the Lukina Padina mine section, whereas VD1 is from the Velin Dol mine section. An. #, analysis number is as in Tables 1 and 2 and Figure 4a,b.

Cobalt, Ni, and Pb have common patterns of distribution. Copper, Ag, Zn, and Cd form another group of elements that show similar distribution patterns in growth zones. Manganese, Zn, and Se are detected in all analyzed spots in constant, but low concentrations: Mn (5–9 ppm), Zn (3–25 ppm), and Se (4–21 ppm).

Single significantly higher concentrations of Zn coincide with elevated contents of Cu, Ag, and Cd, attesting probably an inclusion of tetrahedrite–tennantite. Such discrete inclusions are visible on Figure 4. Single high concentrations of Cr and Mn can also be attributed to mineral influence. Cadmium, In, Te, and Bi were detected sporadically with concentrations below 1 ppm.

Gold shows strong attachment to colloform pyrite. Although microscopically visible gold was not observed, it was detected in almost all analyzed spots. Its concentration varies from 0.07 to 2.77 ppm, and it was usually around 1 ppm.

## 4.2. Efflorescent Mineral Assemblage

### 4.2.1. Mineralogy

As a result of colloform pyrite rapid oxidation in air, iron sulfate phases start to crystallize on its surface and become macroscopically visible in days or months, depending mostly on the air humidity. In years, colloform pyrite aggregates stored in laboratory conditions (approximately 20–25 °C and 20–40% air humidity), usually disintegrate entirely. Sulfates examined in this study gradually formed on the colloform fractured and polished surfaces over several months and continue to crystallize at the moment. The minerals were identified by XRD, SEM-EDS, and LA-ICP-MS techniques. Table 3 summarizes the identified minerals, their chemical formula, the mineral group and the crystal system affiliation (class and space group), the abundance within the assemblage, and the method of identification. This study acknowledged the presence of gypsum, anhydrite, römerite, szomolnokite, and halotrichite as major minerals. Copiapite, coquimbite, and voltaite group minerals occur as minor and accessory phases.

**Table 3.** Semi-quantitative mineral composition of efflorescent aggregates determined by XRD and SEM-EDS: major mineral (>3%)—M; minor mineral (1–3%)—m, accessory mineral (<1%)—a.

Mineral	Class and Space Group	Content (%)	Method
<i>Gypsum supergroup</i>			
Gypsum $\text{CaSO}_4 \cdot 2\text{H}_2\text{O}$	Monoclinic–Prismatic $I2/a$	M (14)	XRD, SEM-EDS
Anhydrite $\text{CaSO}_4$	Orthorhombic–Dipyramidal $Amma$	M (27)	XRD
Römerite $\text{Fe}^{2+}\text{Fe}^{3+}_2(\text{SO}_4)_4 \cdot 14\text{H}_2\text{O}$	Triclinic–Pinacoidal $P\bar{1}$	M (21)	XRD, LA-ICP-MS
<i>Kieserite group</i>			
Szomolnokite $\text{Fe}^{2+}\text{SO}_4 \cdot \text{H}_2\text{O}$	Monoclinic–Prismatic $B2/b$	M (33)	XRD, SEM-EDS LA-ICP-MS
<i>Copiapite group</i>			
Copiapite $\text{Fe}^{2+}\text{Fe}^{3+}_4(\text{SO}_4)_6(\text{OH})_2 \cdot 20\text{H}_2\text{O}$	Triclinic–Pinacoidal $P\bar{1}$	m	SEM-EDS LA-ICP-MS
Aluminocopiapite $\text{Al}_{2/3}\text{Fe}^{3+}_4(\text{SO}_4)_6(\text{OH})_2 \cdot 20\text{H}_2\text{O}$	Triclinic–Pinacoidal $P\bar{1}$	m	SEM-EDS
Magnesiocopiapite $\text{MgFe}^{3+}_4(\text{SO}_4)_6(\text{OH})_2 \cdot 20\text{H}_2\text{O}$	Triclinic–Pinacoidal $P\bar{1}$	m (2.6)	XRD LA-ICP-MS
<i>Coquimbite group</i>			
Coquimbite $\text{Fe}^{3+}_2(\text{SO}_4)_3 \cdot 9\text{H}_2\text{O}$	Trigonal–Hexagonal Scalenohehdral $P\bar{3}1c$	a	SEM-EDS
Aluminocoquimbite $\text{AlFe}^{3+}(\text{SO}_4)_3 \cdot 9\text{H}_2\text{O}$	Trigonal–Hexagonal Scalenohehdral $P\bar{3}1c$	a (0.9)	XRD
<i>Voltaite group</i>			
Voltaite $\text{K}_2\text{Fe}^{2+}_5\text{Fe}^{3+}_3\text{Al}(\text{SO}_4)_{12} \cdot 18\text{H}_2\text{O}$	Isometric–Hexoctahedral $Fd\bar{3}c$	m	SEM-EDS LA-ICP-MS
Ammoniomagnesiovoltaite $(\text{NH}_4)_2\text{Mg}^{2+}_5\text{Fe}^{3+}_3\text{Al}(\text{SO}_4)_{12} \cdot 18\text{H}_2\text{O}$	Isometric–Hexoctahedral $Fd\bar{3}c$	a	LA-ICP-MS
<i>Halotrichite group</i>			
Halotrichite $\text{Fe}^{2+}\text{Al}_2(\text{SO}_4)_4 \cdot 22\text{H}_2\text{O}$	Monoclinic–Sphenoidal $P2_1c$	M	SEM-EDS LA-ICP-MS

*Gypsum* and *anhydrite* are observed macroscopically as massive, powder-like creamy-white aggregates. SEM study show that gypsum forms elongated prismatic crystals.

*Halotrichite* occurs on the pyrite surface as radial, divergent, matted aggregates of transparent to white acicular (fiber needle-like) crystals, elongated along (001) (Figure 6a–d). Halotrichite closely associates with voltaite and szomolnokite, which crystallize within its aggregates, on the prismatic faces of the crystals. (Figure 6b–d).

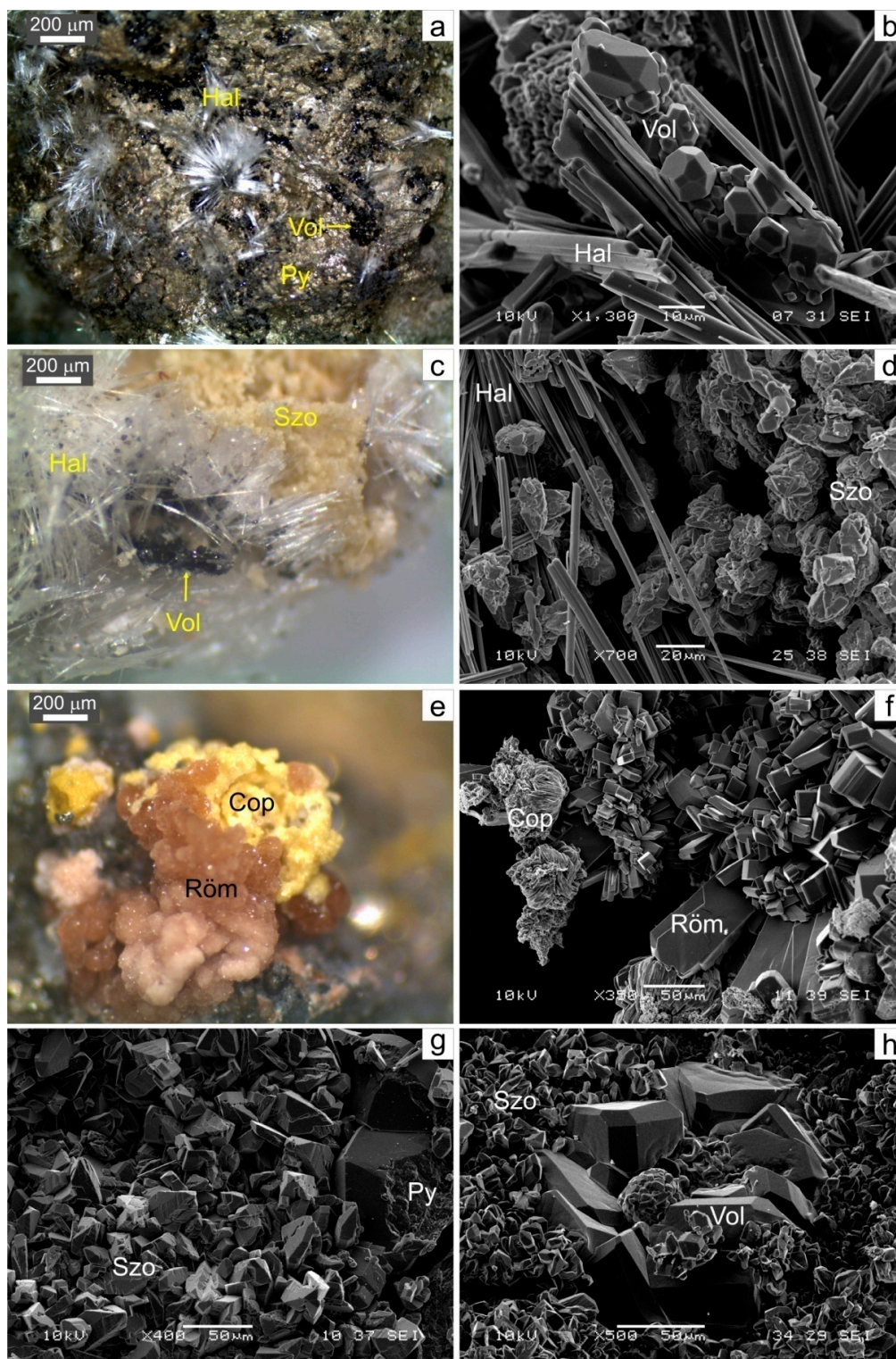


**Figure 6.** (a) Photograph of halotrichite radial aggregates and voltaite (black) on colloform pyrite; (b) SEM secondary electron image (SEI) of voltaite and halotrichite; (c,d) photograph and SEM-SEI of halotrichite and szomolnokite. On (c), voltaite is also visible; (e,f) photograph and SEM-SEI of copiapite–römerite aggregates; (g) SEM-SEI of szomolnokite clusters on pyrite; (h) SEM-SEI of szomolnokite–voltaite aggregates. Abbreviations: Py, pyrite; Hal, halotrichite; Vol, voltaite; Cop, copiapite; Röm, römerite; Szo, szomolnokite.

*Copiapite group minerals* (copiapite, alunocopiapite, and magnesiocopiapite) occur often in association with *römerite* (Figure 6e,f). Copiapite is bright yellow, whereas *römerite* is transparent, forming pale beige to beige-pinkish-colored crystal aggregates. Being triclinic, they occur as platy, tabular crystals on {010} forming clusters of divergent crystals (*römerite*), or contact twins on {010} and {001} to form rosette-like aggregates (copiapite) (Figure 6f).

*Szomolnokite* is the most abundant iron sulfate in the mineral assemblage (33%). It forms creamy, ivory-white fine-grained, “massive” aggregates (Figure 6c). SEM revealed that *szomolnokite* occurs as dense clusters of 5–50- $\mu\text{m}$ -sized distorted pseudo-dipyramidal crystals, which actually represent the complex twinning of prismatic crystals along the elongation axis (Figure 6d,g). The extensive oxidation of pyrite provides a constant source for crystallization, and the twinned crystals are overgrown by new crystals, as the whole scepter-like twin strives to preserve the overall dipyramidal shape (Figure 6d). It also forms ball-shaped clusters of complex twinned crystals (Figure 6h), which is probably a result of bacteria activity.

*Voltaite group minerals* occur as black (voltaite) (Figure 6a,c) to pale olive-green (ammoniomagnesiovoltaite) clusters of well-formed complex cubic crystals with {111} octahedron, {100} cube, and {110} rhombic dodecahedron crystal forms developed to varying degrees (Figure 6b,h).

Complex voltaite twinned aggregates form (1) around one central axis (tetragonal) and grow divergently aside to form an encrustation; (2) around halotrichite needle-shaped crystals to form scepter-like aggregates.

*Coquimbite group minerals* occur as combinations of hexagonal prisms  $\{10\bar{1}0\}$ ,  $\{11\bar{2}0\}$ , dipyramid  $\{10\bar{1}1\}$ , and basal pinacoid {0001}, developed to various degrees (Figure 7). It is mostly transparent in color and associates with copiapite.

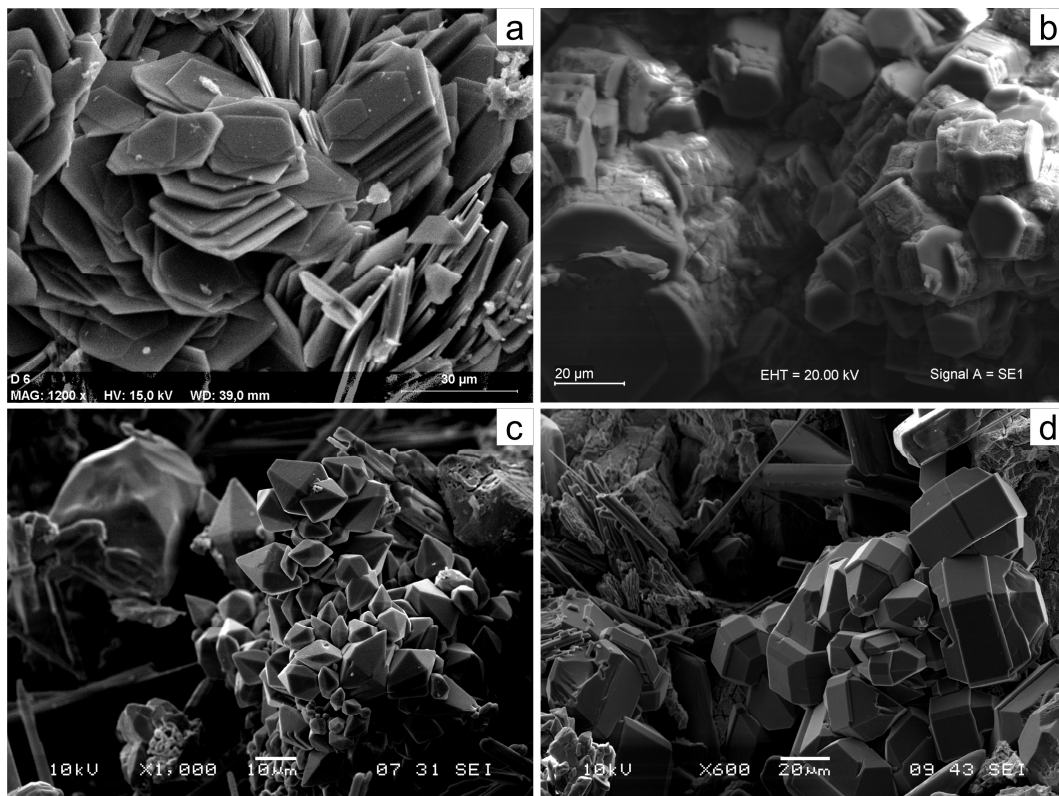


**Figure 7.** SEM-SEI of coquimbite aggregates: (a) hexagonal plates (prism end pinacoid forms); (b) hexagonal prisms; (c) hexagonal dipyramids; (d) complex shape including all previous mentioned forms.

#### 4.2.2. Chemical Composition of the Identified Efflorescent Minerals

The chemical composition of efflorescent minerals was determined in situ on carbon-coated aggregates by EMPA. Representative microprobe analyses of szomolnokite, aluminocopiapite, copiapite, magnesiocopiapite, coquimbite, voltaite, and halotrichite are included in Table 4. Phosphorous and Si were determined in some analyses. Arsenic is present almost everywhere.

**Table 4.** Representative EMPA analyses of sulfates.

Mineral	Na <sub>2</sub> O	K <sub>2</sub> O	MgO	Al <sub>2</sub> O <sub>3</sub>	SiO <sub>2</sub>	CaO	FeOt/ Fe <sub>2</sub> O <sub>3t</sub> *	As <sub>2</sub> O <sub>3</sub>	P <sub>2</sub> O <sub>5</sub>	SO <sub>3</sub>	H <sub>2</sub> O	Sum
szomolnokite	bdl	bdl	bdl	bdl	bdl	bdl	43.73	bdl	bdl	45.77	10.50	100
szomolnokite	bdl	bdl	0.17	bdl	bdl	bdl	44.13	2.31	bdl	42.99	10.40	100
szomolnokite	bdl	bdl	bdl	bdl	bdl	bdl	38.95	bdl	bdl	50.30	10.75	100
szomolnokite	bdl	bdl	bdl	bdl	bdl	bdl	43.09	bdl	bdl	51.74	10.70	100
szomolnokite	bdl	bdl	bdl	bdl	0.42	bdl	41.23	bdl	bdl	48.05	10.30	100
aluminocopiapite	bdl	bdl	0.02	2.86	bdl	bdl	25.87	1.83	bdl	38.22	31.20	100
aluminocopiapite	bdl	bdl	0.02	3.62	bdl	bdl	25.35	2.13	bdl	37.69	31.20	100
aluminocopiapite	bdl	bdl	bdl	6.35	bdl	bdl	23.30	bdl	bdl	39.25	31.10	100
copiapite	bdl	bdl	0.96	bdl	bdl	1.11	28.88	3.68	bdl	34.32	31.15	100
magnesiocopiapite	bdl	bdl	3.15	bdl	bdl	bdl	23.13	bdl	bdl	42.72	31.00	100
coquimbite	1.40	0.21	0.42	0.25	2.11	0.32	27.48	0.36	bdl	38.60	29.85	100
coquimbite	2.70	bdl	0.26	bdl	bdl	bdl	27.95	0.85	bdl	39.35	29.90	100
coquimbite	bdl	bdl	bdl	5.41	bdl	bdl	18.98	0.57	bdl	46.18	29.85	100
coquimbite	bdl	bdl	bdl	3.65	bdl	bdl	22.00	bdl	bdl	45.34	29.00	100
voltaite	bdl	1.01	0.96	2.05	0.46	0.25	32.86	1.18	3.35	41.88	16.00	100
voltaite	bdl	1.68	bdl	4.36	bdl	bdl	37.00	bdl	bdl	41.06	15.90	100
voltaite	bdl	2.53	0.63	2.66	0.40	bdl	26.99	1.46	0.54	48.69	16.10	100
voltaite	bdl	1.32	0.58	2.76	0.35	bdl	29.39	bdl	bdl	49.65	15.96	100
voltaite	bdl	1.40	0.67	3.28	bdl	0.14	28.78	bdl	bdl	49.80	15.93	100
voltaite	bdl	2.02	0.47	3.20	bdl	bdl	28.28	bdl	bdl	50.02	16.00	100
halotrichite	bdl	bdl	bdl	7.13	bdl	bdl	9.73	bdl	bdl	40.14	43.00	100

H<sub>2</sub>O—by difference; bdl, below detection limits. \* Iron content is given as FeOt for szomolnokite and halotrichite; and as Fe<sub>2</sub>O<sub>3t</sub> for copiapite, aluminocopiapite, magnesiocopiapite, coquimbite, and voltaite.

Trace element composition was determined by LA-ICP-MS on gently pressed fiber aggregates of halotrichite and monomineral crystal aggregates of szomolnokite, römerite, copiapite, and voltaite varieties. The estimated concentrations are given in Table 5. This method identified the presence of ammoniomagnesiovoltaite. Although the ammonium content obviously cannot be measured by LA-ICP-MS, the content of other elements coincides with those reported in [53]. All analyses show that sulfate minerals contain not only inherited elements from pyrite, but also new introduced elements. The inherited trace elements are Cr, Fe, Co, Ni, Cu, Zn, Ag, In, As, Sb, Hg, Tl, and Pb. The newly introduced elements are Na, Mg, Al, Si, P, K, Ca, Sc, Ti, V, Mn, Ga, Rb, Sr, Y, Zr, Sn, Cs, Ba, REE (La, Ce, Nd, Sm, Eu), U, and Th. Gold was not detected in sulfates. The most hazardous elements (As, Sb, Tl, and Hg, excluding Pb) were included in the new minerals. Among these, Hg is least incorporated in sulfates. The others occur in reduced concentrations. Silver was detected only in halotrichite and szomolnokite. However, these concentrations could have been higher depending on the colloform pyrite source.

Therefore, it can be assumed that As, Sb, and Tl are entirely inherited in the efflorescent sulfates. The same can be suggested for Co, Ni, Cu, Zn, and Cd. They occur as concentrations commensurable to those detected in pyrite.

Sodium, Mg, and Mn were determined in all sulfates. Aluminum is absent in szomolnokite and magnesiocopiapite, whereas Cs was determined in copiapite and magnesiocopiapite. Voltaite group minerals incorporate most of the trace elements, including the rarest P, Si, V, Rb, Y, Zr, REE, U, and Th. The concentrations of trace elements in sulfate minerals vary spatially based on the colloform pyrite-bearing assemblage that is involved in the oxidation.

**Table 5.** Element concentrations (ppm) of sulfate minerals determined by LA-ICP-MS.

Element	Hal	Hal	Hal	Vol	Vol	Vol	Vol	NH <sub>4</sub> -Mg-Vol	NH <sub>4</sub> -Mg-Vol	NH <sub>4</sub> -Mg-Vol	Szo	Szo
Na	151	142	118	22.9	61.4	748	484	505	323	354	263	257
Mg	880	1139	985	3338	2000	25,903	28,544	33,821	39,981	39,730	420	239
Al	78,559	81,867	61,641	20,917	20,243	20,898	20,896	16,456	16,535	16,743	bdl	bdl
Si	bdl	bdl	bdl	bdl	4118.61	bdl	bdl	bdl	bdl	bdl	bdl	bdl
P	bdl	bdl	bdl	538	812	7011	6849	378	468	480	bdl	bdl
K	184	bdl	209	31,284	29,306	16,754	11,496	1018	bdl	255	bdl	bdl
Ca	bdl	bdl	bdl	bdl	bdl	bdl	bdl	4758	bdl	bdl	bdl	bdl
Sc	bdl	bdl	bdl	bdl	bdl	140.66	89.47	14.9	bdl	15.24	bdl	bdl
Ti	265	bdl	bdl	68.4	bdl	bdl	bdl	bdl	bdl	bdl	bdl	bdl
V	bdl	bdl	3.1	9.0	8.5	14.5	14.7	10.2	7.3	7.0	bdl	bdl
Cr	bdl	bdl	73.5	bdl	bdl	bdl	bdl	bdl	bdl	36.7	bdl	bdl
Mn	19.6	21.6	20.6	75.3	65.8	519	575	14,377	11,920	15,306	101	82.2
Fe	62,700	62,700	62,700	220,200	220,200	187,700	176,900	131,300	133,400	131,800	328,700	328,700
Co	337	378	353	149	100	217	230	15.2	19.6	17.1	77.2	69.6
Ni	1151	1174	1274	146	127	987	1008	73.3	173	154	72.5	86.9
Cu	96.4	95.2	156	108	78.5	361	458	77.2	65.8	74.8	139	157
Zn	bdl	bdl	bdl	14.9	13.3	128	137	40.2	44.0	36.3	bdl	bdl
Ga	12.0	bdl	13.3	bdl	bdl	bdl	bdl	bdl	bdl	3.35	bdl	bdl
As	1462	1207	1213	1120	2287	16,634	13,754	11,082	9353	11,953	1464	1308
Rb	bdl	bdl	bdl	182	183	63.6	53.4	5.1	bdl	bdl	bdl	bdl
Sr	1.19	bdl	bdl	bdl	bdl	bdl	bdl	3.7	0.59	1.0	bdl	bdl
Y	bdl	bdl	bdl	2.3	1.9	73.8	30.7	1.5	1.7	1.3	bdl	bdl
Zr	1.9	bdl	0.65	14.5	12.3	8.8	6.3	4.7	bdl	bdl	bdl	bdl
Ag	1.1	bdl	12.5	bdl	bdl	bdl	bdl	bdl	bdl	bdl	2.1	bdl
Cd	bdl	bdl	bdl	bdl	bdl	bdl	9.90	13.3	bdl	bdl	bdl	bdl
In	bdl	bdl	bdl	bdl	bdl	0.96	0.70	bdl	0.28	0.54	bdl	bdl
Sn	bdl	bdl	bdl	bdl	bdl	bdl	bdl	bdl	bdl	bdl	bdl	bdl
Sb	28.6	11.7	30.1	22.4	21.2	450	304	413	172	246	110	81.5
Cs	1.1	1.1	0.56	3.9	5.6	3.7	6.4	8.4	10.4	10.9	0.93	0.61
Ba	bdl	bdl	bdl	bdl	4.32	bdl	bdl	16.2	bdl	bdl	bdl	bdl
La	bdl	bdl	bdl	bdl	bdl	bdl	bdl	0.52	0.66	bdl	bdl	bdl
Ce	bdl	bdl	bdl	1.0	1.0	bdl	0.47	2.6	2.0	2.0	bdl	bdl
Nd	bdl	bdl	bdl	bdl	bdl	7.0	bdl	bdl	bdl	bdl	bdl	bdl
Sm	bdl	bdl	bdl	bdl	bdl	6.7	3.4	bdl	bdl	bdl	bdl	bdl
Eu	bdl	bdl	bdl	bdl	bdl	4.4	1.6	bdl	bdl	bdl	bdl	bdl
Hg	1.7	4.6	1.3	2.1	1.2	2.2	3.1	6.8	bdl	1.1	1.7	0.60
Tl	bdl	bdl	bdl	377	508	1378	1646	34.2	17.6	24.2	4.9	4.4
Pb	4.4	bdl	bdl	1.5	2.5	8.3	8.1	214	80.5	48.2	9.6	5.8
Th	bdl	bdl	bdl	1.6	2.4	bdl	bdl	bdl	bdl	bdl	bdl	bdl
U	bdl	bdl	bdl	7.6	3.5	bdl	bdl	bdl	0.25	bdl	bdl	bdl

Table 5. Cont.

Element	Röm	Röm	Röm	Cop	Cop	Cop	Cop	Mg-Cop	Mg-Cop	Mg-Cop	Mg-Cop
Na	20.4	bdl	16.0	23.5	17.1	bdl	bdl	bdl	bdl	88.2	bdl
Mg	173	153	221	5676	5596	5686	5989	16,312	20,904	20,453	21,213
Al	132	104	163	862	1129	775	792	1337	bdl	bdl	171
Si	bdl										
P	bdl										
K	bdl										
Ca	bdl										
Sc	bdl										
Ti	bdl										
V	50.0	71.4	54.7	8.3	5.6	bdl	bdl	9.9	bdl	bdl	bdl
Cr	96.2	92.0	157	bdl	bdl	bdl	bdl	28.2	bdl	bdl	bdl
Mn	94.8	165	125	45.1	42.6	45.7	48.3	497	714	778	664
Fe	209,200	209,200	209,200	223,400	223,400	223,400	223,400	183,300	183,300	183,300	183,300
Co	37.4	32.0	36.8	399	440	439	443	69.0	bdl	bdl	bdl
Ni	177	136	252	1254	1361	1492	1551	957	bdl	bdl	bdl
Cu	659	524	530	114	115	130	140	30.0	bdl	bdl	bdl
Zn	bdl	bdl	bdl	17.2	19.6	28.0	20.4	19.3	bdl	bdl	bdl
Ga	bdl	1.9	bdl	bdl	bdl						
As	474	417	557	266	361	209	797	30.1	9021	8155	6712
Rb	bdl										
Sr	bdl										
Y	bdl										
Zr	bdl	bdl	0.72	bdl							
Ag	bdl										
Cd	bdl										
In	bdl	bdl	bdl	0.35	0.29	0.30	0.30	0.29	bdl	bdl	bdl
Sn	14.2	16.3	25.1	bdl							
Sb	52.1	49.5	71.8	162	216	164	927	5.2	1156	1208	809
Cs	1.1	0.70	1.2	bdl	bdl	bdl	0.68	bdl	1.6	2.2	bdl
Ba	bdl										
La	bdl										
Ce	bdl										
Nd	bdl										
Sm	bdl										
Eu	bdl										
Hg	bdl	bdl	0.66	1.9	1.6	0.72	2.0	0.35	bdl	bdl	1.2
Tl	0.44	0.34	0.69	0.60	0.86	2.06	10.6	bdl	37.6	39.2	24.2
Pb	bdl	bdl	0.52	bdl	bdl	bdl	1.4	bdl	bdl	bdl	bdl
Th	bdl										
U	bdl										

bdl, below detection limits. Mineral abbreviations: Hal, halotrichite; Vol, voltaite; NH<sub>4</sub>-Mg-Vol, ammoniomagnesiovoltaite; Szo, szomolnokite; Röm, römerite; Cop, copiapite; Mg-Cop, magnesiocopiapite.

## 5. Discussion

### 5.1. Colloform Pyrite Chemistry: Mode of Occurrence of Trace Elements and Genetic Implications

Based on the flat down-hole ablation profiles of As and Sb, and their negative correlations to S (As,  $r = -0.66$ ; Sb,  $r = -0.34$ ; As + Sb,  $r = 0.59$ ), a typical  $As^-$ ,  $Sb^-$  substitution for S exists. However, their negative correlations with Fe (As,  $r = -0.58$ ; Sb,  $r = -0.42$ ) could suggest also the presence of heterovalent substitutions of As and Sb for Fe [16,54], although they are not well defined. Arsenic and Sb show common distribution patterns with Tl and Hg in growth zones (Figure 5), as well as strong positive correlations ( $r > 0.75$ ), whereas Tl and Hg correlate negatively toward Fe ( $r = -0.34$  and  $-0.64$ , respectively). This could denote a coupled substitution  $2Fe^{2+} \leftrightarrow M^{3+} + Tl^+$ , where  $M^{3+}$  are  $As^{3+}$  and  $Sb^{3+}$ . Such substitution mechanisms were suggested by [55,56] and proved by [57]. The stronger positive correlation between Tl and Sb ( $r = 0.98$ ), than Tl with As ( $r = 0.75$ ) supports a predominant  $Sb^{3+} + Tl^+$  coupled substitution.

Mercury contents in pyrite were reported mostly for colloform and framboidal varieties that occur in sedimentary environments ([58,59] and references therein) and Carlin-type [2,15,60,61] deposits. Its occurrence in pyrite is usually related to As-rich zones, because As-rich pyrites imply non-stoichiometric substitutions, which distort the crystal structure and require charge balance (semi-conducting behavior [1,62]). This could be achieved in colloform pyrite by incorporating other metal cations or even nanoparticulate minerals, as it was reported by [55,61]. Here, the positive correlation of Hg and As, and the negative correlation with Fe ( $r = -0.64$ ), as well as the flat down-hole ablation profiles suggest that Hg could occur as an isovalent substitution for Fe within As-rich growth zones. Since cinnabar is also observed in the assemblage, a nanoparticulate form within colloform pyrite is also very possible.

Cobalt and Ni isovalent substitutions for Fe in pyrite lattice are examined as solid solution [63] and discussed in [1,64]. In this study, Co and Ni show similar distribution patterns and strong positive correlation with Pb ( $r = 0.73$  and  $0.90$ , respectively). Negative correlations of Co, Ni, and Pb with Fe are insignificant to missing. Such correlations suggest the presence as nanoparticulate form rather than substitution. Galena occurs within the colloform pyrite-bearing assemblage; thus, it is more likely that it was attached to the growing surfaces of colloform pyrite and overgrown. Higher Co and Ni contents for this colloform pyrite, as well as cobaltian polydymite, were reported by [38].

Gold content does not show particular dependence on the As content, or strong association with other trace elements, excluding Se ( $r = 0.50$ ). Weak ( $r = 0.35$ ) positive correlations are established with Co, Ni, and Pb. Although the contents of Au and As plot well below the solubility limit defined by [15], suggesting its presence as structurally bound species, the absence of any correlation with As, and the association with Co, Ni, Pb, and Se argues for nanoparticulate presence. Gold apparently comes with fluid portions enriched with Co, Ni, Pb, and Se, and deposits predominantly as  $Au^0$  [61], rather than  $Au^+$  in coupled substitution with  $As^{3+}$  [16,54]. It is possible to form nanoparticulate Au–Se phases.

Well-defined positive correlations exist among Cu, Ag, Zn, and Cd ( $r = 0.78$ – $0.97$ ), which show similar distribution patterns in growth zones (Figure 5). Copper and Zn have weak to insignificant positive correlations with Pb. Correlation with Fe is missing. This fact refers their relation to nano- to micron-sized inclusions of tetrahedrite–tennantite or chalcopyrite together with galena. Tellurium, Bi, and In were detected in very low concentrations. They are probably related to galena or tetrahedrite–tennantite.

The trace element signature of colloform pyrite (enrichment with As, Sb, Hg, and Tl) is characteristic for the low-temperature final stages of hydrothermal activity in the ore zone ( $<200$  °C) [65,66]. The colloform pyrite precipitated from supersaturated sulfide-rich fluids with almost constant As activity and pulses enriched with Sb, Hg, Tl, Au, Ag, Ni, Co that were buffered by the calcite and siderite marble host rocks. The supersaturation of the fluid allowed crystallization from multiple nucleation centers. The nucleation of other mineral phases occurred on the rough surface of the rapidly growing acicular crystals with unbalanced chemical composition. The charge deficiency

caused by As and other cations substituting in the crystal lattice could have attracted the deposition of nanoparticulate Au and other minerals, such as galena, tetrahedrite–tennantite, cinnabar, and possibly polydymite. The mineralization precipitated from evolved hydrothermal fluid (intrusion derived mixed with heated meteoric water), which interacted additionally with the country rocks along faults before depositing in the calcite–siderite marble bodies.

## 5.2. Transformation Mechanisms

Pyrite oxidation mechanism has been studied extensively in several experimental studies simulating natural environmental conditions—in air, water solutions with different pH and the presence of carbonates [20–24]. [20,23] inferred that the rate of oxidation is a linear function of the pyrite surface area. Pyrites composed by micron- to submicron-sized crystals with porous texture (framboidal and colloform) naturally possess high surface area that would react during oxidation, causing more rapid transformation (physical and chemical). [23] summarized the oxidation in water solution in two reactions: (1)  $\text{FeS}_2 + 3.5\text{O}_2 + \text{H}_2\text{O} = \text{Fe}^{2+} + 2\text{H}^+ + 2\text{SO}_4^{2-}$ ; (2)  $\text{FeS}_2 + 14\text{Fe}^{3+} + 8\text{H}_2\text{O} = 15\text{Fe}^{2+} + 16\text{H}^+ + 2\text{SO}_4^{2-}$ . These reactions are in part applicable for oxidation in air. [24,67] suggested that the fracturing of the pyrite in air ruptures the S–S bonds and enhances the production of  $\text{Fe}^{3+}$  and  $\text{S}^{2-}$  surface species. Thus, it is possible that ferrous and ferric ions exist concurrently and are incorporated in the formation of szomolnokite and coquimbite. The oxidation of the rough porous surface of the fractured colloform pyrite in air (30–40% humidity) will produce micron-sized supersaturated acidic salt vapor droplets (with  $\text{H}_2\text{SO}_4$ ), from which precipitates rapidly szomolnokite (?) as shapeless masses, coquimbite as micron-sized hexagonal plates, and pseudorombohedral copiapite (Figure 8a,b). The crystal growth promotes the further weathering and fracturing of pyrite (Figure 8b).

The oxidation of pyrite adjacent to carbonate matter (vein calcite or marble particles) will be neutralized by the formation of gypsum and anhydrite and release some Mg. Sericite and chlorite that occur in small quantity in marbles will be affected by the acidic droplets (sulfuric acid) and release K, Al, Si, Mg, and Fe. The trace elements in pyrite are released in the same way. For example, the substitution  $\text{As}^-$  for  $\text{S}^{2-}$  naturally occurring in pyrite can be represented in the following simple reaction:  $\text{FeAs}^- \text{S}^{2-} + 4\text{O}_2 + \text{H}_2\text{O} = \text{Fe}^{2+} + 2\text{H}^+ + \text{SO}_4^{2-} + \text{AsO}_4^{3-}$ , where  $\text{As}^-$  is oxidized to  $\text{As}^{5+}$  and is incorporated as tetrahedral oxyanion. The growth zones that accommodate  $\text{As}^{3+}\text{Tl}^+$  or  $\text{Sb}^{3+}\text{Tl}^+$  substitutions for Fe will require the transfer of less electrons to oxidize the cations to  $\text{As}^{5+}$  and  $\text{Sb}^{5+}$ . Therefore, these growth zones will oxidize more rapidly. Thallium will probably preserve its monovalent oxidation state, which is typical for most environments [68]. The metallic cations that are substituted for Fe in pyrite, as well as newly introduced and oxidized, are incorporated in  $\text{MO}_6$  octahedra, where M is divalent or trivalent cations ( $\text{Fe}^{2+}$ ,  $\text{Mn}^{2+}$ ,  $\text{Mg}^{2+}$ ,  $\text{Zn}^{2+}$ ,  $\text{Al}^{3+}$ ,  $\text{Fe}^{3+}$ , etc.) [69].

Sulfates started to precipitate and grow on the pyrite surface. Halotrichite hardly touched the pyrite surface and crystallized in the fracture open space or over the pyrite surface. This suggests that the immediate air layer above the pyrite surface contains a dense aerosol of liquid salty droplets from which halotrichite crystallizes. Its crystals serve as a nucleation surface for voltaite and szomolnokite (Figure 6). The oxidation of pyrite is probably facilitated by acidophilic bacteria, such as *T. ferrooxidans* and *L. ferrooxidans* ([70] and references therein). *T. ferrooxidans* was reclassified to *Acidithiobacillus ferrooxidans* (*A. ferrooxidans*) in 2000 [71]. The formation of sphere-shaped szomolnokite aggregates (Figure 6h) could be evidence of their activity. The existence of efflorescences is controlled by water vapor in air. If air humidity increases, the supersaturation of the salty liquid droplets decreases and dissolution of the precipitated phases occurs. Dissolution affects the edges of the crystals (copiapite and römerite), less developed crystal faces (szomolnokite), down a trigonal prism-shaped pits on dipyrnidal faces in coquimbite (Figure 8c–f). Our observations show that the order of sulfate crystallization is similar to that described in [25,26]: ferrous (szomolnokite and halotrichite) to ferrous–ferric (copiapite, römerite, and voltaite) and ferric sulfates (coquimbite).

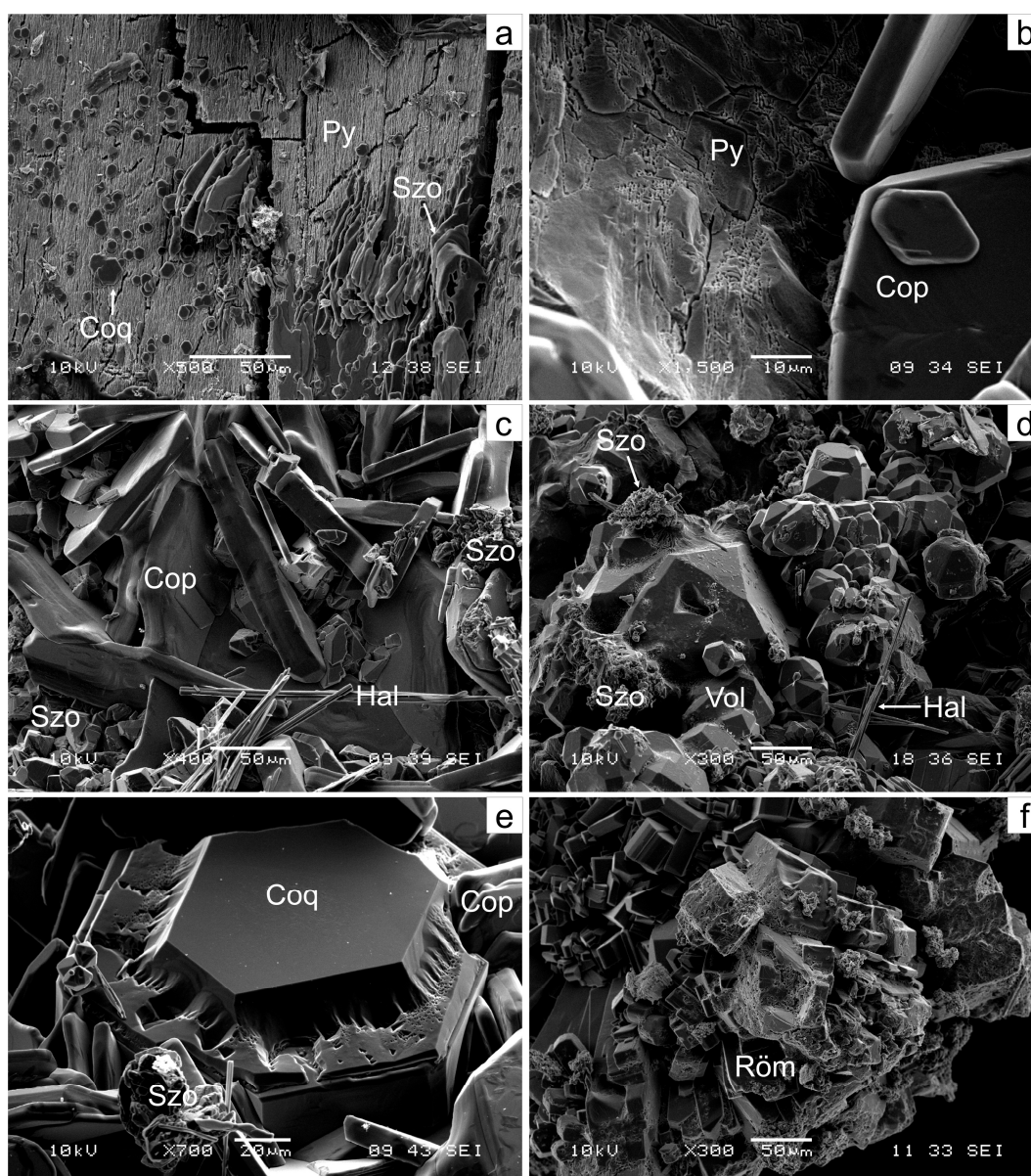


**Figure 8.** Crystallization and dissolution: (a) crystallization of hexagonal coquimbite plates on pyrite porous surface, and the deposition of shapeless szomolnokite mass in fractures; (b) dissolution pits along growth surface of colloform pyrite; (c) rounding off the edges of copiapite crystals, associating with halotrichite and szomolnokite; (d) dissolution of szomolnokite overgrowing voltaite; (e) dissolution of coquimbite (trigonal prism-shaped pits on dipyramidal faces); (f) crystal edge and face dissolution of römerite. Abbreviations: Py, pyrite; Hal, halotrichite; Vol, voltaite; Cop, copiapite; Röm, römerite; Szo, szomolnokite; Coq, coquimbite.

### 5.3. Partitioning of Inherited Trace Elements in Sulfates

The element budget inherited from pyrite is distributed among sulfate phases. Figure 9 shows the trace element concentrations of sulfates normalized to the mean content of trace elements in colloform pyrite. The plot discriminates the element affinity toward particular sulfate phases. The sulfate/mean pyrite <1 of Fe is explained with the redistribution of the initial Fe content among the various sulfates. All newly formed sulfates have lower Fe content than pyrite. It can be seen that V, Cr, and Mn came from external sources. Manganese mostly partitions among voltaite, ammoniomagnesiovoltaite, and magnesiocopiapite, where it enters in the  $M^{2+}$  position of  $Fe^{2+}$  as reported by [53,69,72,73]. Nickel and Co show affinity to copiapite, halotrichite, and voltaite, also occurring in  $M^{2+}$ . Copper partitions among

halotrichite, voltaite, szomolnokite, copiapite, and römerite (highest content). Zinc is incorporated in copiapite and voltaite. As it was suggested by [74,75], Cu and Zn occur in the  $M^{2+}$  position. Most of the As is included in voltaite and magnesiocopiapite. Antimony and Tl are related to voltaite and copiapite group minerals. Mercury and Pb enter in voltaite and magnesiocopiapite. Tin also come from external sources and concentrates in römerite. Cadmium and In also enter in voltaite and copiapite. Generally, all elements from Se to Pb are partly resistant to incorporation in sulfates. Notably, Gold and Se stay out of the new phases. Once released from pyrite, Au was not incorporated in the new phases. This supports the presence of Au in nanoparticulate form ( $Au^0$ ). Silver is more reactive in low-temperature environments. It could be included in acanthite, as such, it was also observed as recent exsolution from Ag-rich tetrahedrites in samples containing the main Ag–Pb ore mineralization in Chiprovtsi deposit. The most hazardous elements (As, Sb, and Tl) are incorporated in the efflorescent minerals. Thallium has a large ionic radius [76]; thus, it probably occurs in the position of K in voltaite minerals, whereas in copiapite it probably occurs in the position of  $M^{2+}$ .

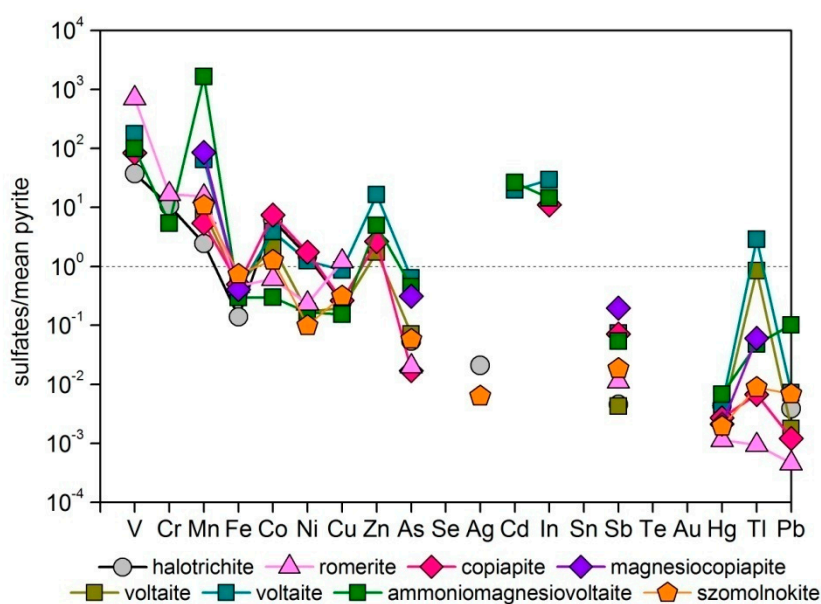


**Figure 9.** Distribution patterns of inherited trace elements among efflorescent sulfates.

#### 5.4. Sources of Introduced Elements in Sulfates and Incorporation

A great number of new elements are introduced in sulfates: Na, Mg, Al, Si, P, K, Ca, Sc, Ti, V, Cr, Mn, Ga, Rb, Sr, Y, Zr, Sn, Cs, Ba, REE (La, Ce, Nd, Sm, Eu), U, and Th. Sources for these elements are other gangue minerals occurring in the mineral assemblage, such as carbonates (calcite and siderite marble particles, and late vein ankerite, calcite), quartz, barite, and fluorite. The host rocks (marbles and chlorite–sericite schists) contain quartz, sericite, and chlorite. The interaction of these minerals with the salty acidic droplets produced by pyrite oxidation releases the following elements: (1) carbonates—Ca, Mg, Mn, Fe, Sr, Ba, and REE; (2) fluorite—Ca, Na, P, Rb, Y, REE, and Cs; (3) barite—Ba, Sr, Rb, and U; (4) sericite—K, Al, Rb, Si, Cs, V, Cr, Ga, Sc, REE, possibly Zr and Sn; (5) chlorite—Al, Mg, Fe, V, Cr, Cs, REE, U, and Th. They are deposited as gypsum, anhydrite, halotrichite, and voltaite. Aluminum and Mg are included as minor constituents in copiapite and coquimbite. The alkaline elements Na, Rb, and Cs, having large ionic radii [76], probably take the position of  $K^+$  in the voltaite group. Scandium probably occurs in the  $Al^{3+}$  position in voltaite. Vanadium and Cr are incorporated in the  $Al^{3+}$  position in halotrichite. Tin, Zr, REE, Y, U, and Th are rarely found mostly in voltaite. Their position is hard to elaborate. REE and Y also have large ionic radii, so they can occur in the K position, or in crystal defects. Tin, Th, and Zr may substitute for  $Al^{3+}$ ,  $Fe^{3+}$ , or  $Mg^{2+}$ , and  $Fe^{2+}$  creating vacancies and electron charges. Uranium in oxidizing conditions forms a uranyl ( $UO_2^{2+}$ ) cation that may occur in

the position of  $\text{Fe}^{2+}$ . Phosphorus occurs as a  $\text{PO}_4^{3-}$  tetrahedral oxyanion. As it is seen, voltaite group minerals incorporate most trace elements, as inferred in [53,72,73].

### 5.5. Environmental Significance

Most of the reported efflorescent mineral formations so far occur in areas associated with (1) ore mining deposition from highly acidic solutions/streams caused by acid mine drainage (AMD) during dry seasons, waste heaps, and dumps [26–30,70,77–80]; (2) coal mining within coal seams and on coal fuel heaps in thermoelectric plants as a result of framboidal pyrite oxidation [81]; (3) natural precipitation from streams during dry seasons on the surface and underground; (4) volcanic and other hydrothermal activity [82], etc. In natural conditions, such formations are subject to periodical dissolution by rainfalls.

Since the newly formed minerals inherit the trace element signature of colloform pyrite, they act as temporary water-soluble carriers before releasing them into the environment when dissolved. Therefore, abundant colloform pyrite in some deposits can become extremely harmful for the areas close to the mines. In this case, colloform pyrite occurrence is very limited. Its association with carbonate host rocks would further restrict its influence on a large scale. However, concentrations of As and Sb were detected in water discharges from abandoned underground mine workings in the Velin Dol and Lukina Padina mine sections, but they do not pose a threat for the Chiprovka Ogosta river flowing through the area [83].

## 6. Conclusions

The oxidation of colloform pyrite aggregates is carried out more rapidly compared to euhedral and anhedral pyrite. The growth zones/bands containing more trace elements react first. The richness of efflorescent mineral assemblage is controlled directly by the mineral composition of the colloform pyrite-bearing assemblage. Most of these minerals take part in the oxidation mechanism and transformation reactions. They act as a source of elements, which do not occur in pyrite, but are essential for the formation of gypsum, anhydrite, halotrichite, voltaite, the Al- and Mg-varieties of copiapite, and coquimbite. The overall order of crystallization starts from ferrous (szomolnokite, halotrichite) to ferrous–ferric (copiapite, römerite, voltaite) and ferric sulfates (coquimbite). Gypsum and anhydrite precipitate as a result of neutralization by the carbonate minerals. The preservation of the efflorescent sulfates is controlled mainly by air humidity; thus, in the laboratory, they continue to grow in relatively steady conditions, with limited dissolution and transformation from one sulfate mineral to another. They form until the entire deterioration of pyrite samples. Most of the trace elements in colloform pyrite are inherited and partitioned among the newly formed phases. Thus, colloform pyrite could be a major cause of environmental pollution.

**Author Contributions:** D.D. and V.M. collected the samples. V.M. and L.H. performed the EMPA analyses and SEM secondary electron images of sulfate minerals. D.D. conducted the LA-ICP-MS analyses of pyrite and sulfate samples, interpreted all the results, and wrote the manuscript. All authors have read and agreed to the published version of the manuscript.

**Funding:** This study was financially supported by the RNF01/0006 and DNTS China01/7 grants of the Bulgarian Science Fund and an exchange mobility grant within the CEEPUS program.

**Acknowledgments:** The authors thank Georgi Avdeev and Martin Tsvetkov (Institute of Physical Chemistry, Bulgarian Academy of Sciences) for their assistance with XRD data acquisition and identification of sulfate phases, and to Tsvetoslav Iliev (Geological Institute, Bulgarian Academy of Sciences) for his help with EMPA analyses of colloform pyrite.

**Conflicts of Interest:** The authors declare no conflict of interest.

## References

1. Abraitis, P.K.; Patrick, R.A.D.; Vaughan, D.J. Variations in the compositional, textural and electrical properties of natural pyrite: A review. *Int. J. Miner. Process.* **2004**, *74*, 41–59. [CrossRef]

2. Barker, S.L.L.; Hickey, K.A.; Cline, J.S.; Dipple, G.M.; Kilburn, M.R.; Vaughan, J.R.; Longo, A. Uncloaking invisible gold: Use of NanoSIMS to evaluate gold, trace elements, and sulfur isotopes in pyrite from Carlin-type gold deposits. *Econ. Geol.* **2009**, *104*, 897–904. [[CrossRef](#)]
3. Cook, N.J.; Ciobanu, C.L.; Mao, J.W. Textural control on gold distribution in As-free pyrite from the Dongping, Huangtuliang and Hougou gold deposits, North China Craton (Hebei Province, China). *Chem. Geol.* **2009**, *264*, 101–121. [[CrossRef](#)]
4. Large, R.R.; Danyushevsky, L.; Hollit, C.; Maslennikov, V.; Meffre, S.; Gilbert, S.; Bull, S.; Scott, R.; Thomas, H.; Singh, B.; et al. Gold and trace element zonation in pyrite using a laser imaging technique: Implications for the timing of gold in orogenic and Carlin-style sediment hosted deposits. *Econ. Geol.* **2009**, *104*, 635–668. [[CrossRef](#)]
5. Reich, M.; Deditius, A.; Chryssoulis, S.; Li, J.-W.; Ma, C.-Q.; Parada, M.A.; Barra, F.; Mittermayr, F. Pyrite as a record of hydrothermal fluid evolution in a porphyry copper system: A SIMS/EMPA trace element study. *Geochim. Cosmochim. Acta* **2013**, *104*, 42–62. [[CrossRef](#)]
6. Wohlgemuth-Ueberwasser, C.C.; Viljoen, F.; Petersen, S.; Vorster, C. Distribution and solubility limits of trace elements in hydrothermal black smoker sulfides: An in-situ LA-ICP-MS study. *Geochim. Cosmochim. Acta* **2015**, *159*, 16–41. [[CrossRef](#)]
7. Keith, M.; Häckel, F.; Haase, K.M.; Schwarz-Schampera, U.; Klemm, R. Trace element systematics of pyrite from submarine hydrothermal vents. *Ore Geol. Rev.* **2016**, *72*, 728–745. [[CrossRef](#)]
8. Sykora, S.; Cooke, D.R.; Meffre, S.; Stephanov, A.S.; Gardner, K.; Scott, R.; Selley, D.; Harris, A.C. Evolution of pyrite trace element compositions from porphyry-style and epithermal conditions at the Lihir gold deposit: Implications for ore genesis and mineral processing. *Econ. Geol.* **2018**, *113*, 193–203. [[CrossRef](#)]
9. Cook, N.J.; Chryssoulis, S.L. Concentration of “invisible gold” in the common sulfides. *Can. Miner.* **1990**, *28*, 1–16.
10. Fleet, M.E.; Chryssoulis, S.L.; MacLean, P.J.; Davidson, R.; Weisener, C.G. Arsenian pyrite from gold deposits: Au and As distribution investigated by SIMS and EMP, and color staining and surface oxidation by XPS and LIMS. *Can. Miner.* **1993**, *31*, 1–17.
11. Fleet, M.E.; Mumin, H. Gold-bearing arsenian pyrite and marcasite and arsenopyrite from Carlin Trend gold deposits and laboratory synthesis. *Am. Miner.* **1997**, *82*, 182–193. [[CrossRef](#)]
12. Maddox, L.M.; Bancroft, G.M.; Scaini, M.J.; Lorimer, J.M. Invisible gold: Comparison of Au deposition on pyrite and arsenopyrite. *Am. Miner.* **1998**, *83*, 1240–1245. [[CrossRef](#)]
13. Simon, G.; Huang, H.; Penner-Hahn, J.E.; Kesler, S.E.; Kao, L.S. Oxidation state of gold and arsenic in gold-bearing arsenian pyrite. *Am. Miner.* **1999**, *84*, 1071–1079. [[CrossRef](#)]
14. Palenik, C.S.; Utsunomiya, S.; Reich, M.; Kesler, S.E.; Ewing, R.C. Invisible gold revealed: Direct imaging of gold nanoparticles in a Carlin-type deposit. *Am. Miner.* **2004**, *89*, 1359–1366. [[CrossRef](#)]
15. Reich, M.; Kesler, S.E.; Utsunomiya, S.; Palenik, C.S.; Chryssoulis, S.L.; Ewing, R.C. Solubility of gold in arsenian pyrite. *Geochim. Cosmochim. Acta* **2005**, *69*, 2781–2796. [[CrossRef](#)]
16. Deditius, A.P.; Reich, M.; Kesler, S.E.; Utsunomiya, S.; Chryssoulis, C.L.; Walshe, J.; Ewing, R.C. The coupled geochemistry of Au and As in pyrite from hydrothermal ore deposits. *Geochim. Cosmochim. Acta* **2014**, *140*, 644–670. [[CrossRef](#)]
17. Vikentyev, I.V. Invisible and microscopic gold in pyrite: Methods and new data for massive sulfide ores of the Urals. *Geol. Ore Depos.* **2015**, *57*, 237–265. [[CrossRef](#)]
18. Trigub, A.L.; Tagirov, B.R.; Kvashnina, K.O.; Chareev, D.A.; Nickolsky, M.S.; Shiryaev, A.A.; Baranova, N.N.; Kovalchuk, E.V.; Mokhov, A.V. X-ray spectroscopy study of the chemical state of “invisible” Au in synthetic minerals in the Fe-As-S system. *Am. Miner.* **2017**, *102*, 1057–1065.
19. Moller, P.; Kersten, G. Electrochemical accumulation of visible gold on pyrite and arsenopyrite surfaces. *Miner. Depos.* **1994**, *29*, 404–413. [[CrossRef](#)]
20. Nicholson, R.V.; Gillham, R.W.; Reardon, E.J. Pyrite oxidation in carbonate-buffered solution: 1. Experimental kinetics. *Geochim. Cosmochim. Acta* **1988**, *52*, 1077–1085. [[CrossRef](#)]
21. Nicholson, R.V.; Gillham, R.W.; Reardon, E.J. Pyrite oxidation in carbonate-buffered solution: 2. Rate control by oxide coating. *Geochim. Cosmochim. Acta* **1990**, *54*, 395–402. [[CrossRef](#)]
22. Moses, C.O.; Herman, J.S. Pyrite oxidation at circumneutral pH. *Geochim. Cosmochim. Acta* **1991**, *55*, 471–482. [[CrossRef](#)]

23. Rimstidt, J.D.; Vaughan, D.J. Pyrite oxidation: A state-of-the-art assessment of the reaction mechanism. *Geochim. Cosmochim. Acta* **2003**, *67*, 873–880. [[CrossRef](#)]
24. Todd, E.C.; Sherman, D.M.; Purton, J.A. Surface oxidation of pyrite under ambient atmospheric and aqueous (pH = 2 to 10) conditions: Electronic structure and mineralogy from X-ray absorption spectroscopy. *Geochim. Cosmochim. Acta* **2003**, *67*, 881–893. [[CrossRef](#)]
25. Buurman, P. In vitro weathering products of pyrite. *Geol. Mijnvouw* **1975**, *54*, 101–105.
26. Nordstrom, D.K.; Alpers, C.N. Negative pH, efflorescent mineralogy, and consequences for environmental restoration at the Iron Mountain Superfund site, California. *Proc. Natl. Acad. Sci. USA* **1999**, *96*, 3455–3462. [[CrossRef](#)]
27. Jambor, J.J.; Nordstrom, D.K.; Alpers, C.N. Metal-sulfate salts from sulfide mineral oxidation. *Rev. Miner. Geochem.* **2000**, *40*, 303–350. [[CrossRef](#)]
28. Buckby, T.; Black, S.; Coleman, M.L.; Hodson, M.E. Fe-sulphate-rich evaporative mineral precipitates from the Rio Tinto, southwest Spain. *Miner. Mag.* **2003**, *67*, 263–278. [[CrossRef](#)]
29. Jerz, J.K.; Rimstidt, J.D. Efflorescent iron sulfate minerals: Paragenesis, relative stability, and environmental impact. *Am. Miner.* **2003**, *88*, 1919–1932. [[CrossRef](#)]
30. Buzatu, A.; Dill, H.G.; Buzgar, N.; Damian, G.; Maftei, A.E.; Apopei, A.I. Efflorescent sulfates from Baia Sprie mining area (Romania)—Acid mine drainage and climatological approach. *Sci. Total Environ.* **2016**, *542*, 629–641. [[CrossRef](#)]
31. Bonev, I.K.; Reiche, M.; Marinov, M. Morphology, perfection and growth of natural pyrite whiskers and thin platelets. *Phys. Chem. Miner.* **1985**, *12*, 223–232. [[CrossRef](#)]
32. Chen, T.T. Colloform and framboidal pyrite from the Caribou deposit, New Brunswick. *Can. Miner.* **1978**, *16*, 9–15.
33. Ohfuji, H.; Rickard, D. Experimental syntheses of framboids—A review. *Earth-Sci. Rev.* **2005**, *71*, 147–170. [[CrossRef](#)]
34. Bonev, I.K.; Atanassova, R. Crystallography and origin of colloform pyrite. In Proceedings of the IMA 2006, Kobe, Japan, 23–28 July 2006; p. 174.
35. Barrie, C.D.; Boyce, A.J.; Boyle, A.P.; Williams, P.J.; Blake, K.; Ogawara, T.; Akai, J.; Prior, D.J. Growth controls in colloform pyrite. *Am. Miner.* **2009**, *94*, 415–429. [[CrossRef](#)]
36. Atanassova, R. Environmental significance of pyrite with colloform textures. *C. R. Acad. Bulg. Sci.* **2010**, *63*, 1335–1340.
37. Gao, S.; Huang, F.; Wang, Y.; Gao, W. A review of research progress in the genesis of colloform pyrite and its environmental indications. *Acta Geol. Sin.* **2016**, *90*, 1353–1369.
38. Atanassov, V.; Pavlov, I. Notes about mineralogy and paragenetic zoning of minerals deposits in Chiprovtsi ore region. *Ann. Ecol. Sup. Miner. Geol.* **1983**, *28*, 159–178. (In Bulgarian)
39. Tarasova, E.; Tarassov, M. Horizontal zonality and mineral composition of skarns in the Martinovo deposit. *Geochem. Miner. Pet.* **1988**, *24*, 68–76. (In Bulgarian)
40. Carrigan, C.W.; Mukasa, S.B.; Haydoutov, I.; Kolcheva, K. Age of Variscan magmatism from the Balkan sector of the orogen, Central Bulgaria. *Lithos* **2005**, *82*, 125–147. [[CrossRef](#)]
41. Amov, B.; Arnaudov, V.; Pavlova, M.; Dragov, P.; Baldjieva, T.; Evstatieva, S. Lead isotope data on the Paleozoic granitoids and ore mineralizations from the Western Balkan Mountains and the Tran district (West Bulgaria). I. Isotopic ratios and geochronology. *Geol. Balc.* **1981**, *11*, 3–26.
42. Dragov, P.; Galiy, S.A.; Zhukov, F.I. Carbon, oxygen and sulfur isotopes in minerals from the Chiprovtsi ore zone. *Rev. Bulg. Geol. Soc.* **1991**, *52*, 50–61. (In Bulgarian)
43. Haydoutov, I. Precambrian ophiolites, Cambrian island arc and Variscan suture in South Carpathian-Balkan region. *Geology* **1989**, *17*, 905–908. [[CrossRef](#)]
44. Haydoutov, I. *Origin and Evolution of the Precambrian Balkan-Carpathian Ophiolite Segment*; BAS Press: Sofia, Bulgaria, 1991; p. 179. (In Bulgarian)
45. Haydoutov, I.; Yanev, S. The Protomoesian microcontinent of the Balkan Peninsula—A peri-Gondwanian piece. *Tectonophysics* **1997**, *272*, 303–313. [[CrossRef](#)]
46. Plissart, G.; Monnier, C.; Diot, H.; Maruntiu, M.; Berger, J.; Triantafyllou, A. Petrology, geochemistry and Sm-Nd analyses on the Balkan-Carpathian Ophiolite (BCO—Romania, Serbia, Bulgaria): Remnants of a Devonian back-arc basin in the easternmost part of the Variscan domain. *J. Geodyn.* **2017**, *105*, 27–50. [[CrossRef](#)]

47. Dragov, P.; Obretenov, N. Morphology and genesis of the siderite bodies in the Chiprovtsi deposit. *Bull. Geol. Inst. Ser. Met. Non-Met. Miner. Depos.* **1972**, *21*, 37–53.
48. Obretenov, N. The Chiprovtsi ore field—Chiprovtsi deposit. In *Lead-Zinc Deposits in Bulgaria*; Technika: Sofia, Bulgaria, 1988; pp. 193–206.
49. Milev, V.; Stanev, V.; Ivanov, V. The Extracted Ores in Bulgaria during 1878–1995—Statistical Reference Book. *Sofia Zemya* **1996**, *93*, 196. (In Bulgarian)
50. Angelov, V.; Antonov, M.; Gerdzhikov, S.; Aydanlyiski, G.; Petrov, P.; Kisselinov, H. *Geological Map of Bulgaria M 1:50000, Map Sheet “Chiprovtsi”*; Ministry of Environment and Water, Bulgarian Geological Survey: Sofia, Bulgaria, 2008.
51. Wilson, S.A.; Ridley, W.I.; Koenig, A.E. Development of sulfide calibration standards for the laser ablation inductively-coupled plasma mass spectrometry technique. *J. Anal. At. Spectrom.* **2002**, *17*, 406–409. [[CrossRef](#)]
52. Guillong, M.; Meier, D.L.; Allan, M.M.; Heinrich, C.A.; Yardley, B.W.D. Appendix A6: SILLS: A MATLAB-based program for the reduction of laser ablation ICP-MS data of homogeneous materials and inclusions. In *Laser Ablation ICP-MS in the Earth Sciences: Current Practices and Outstanding Issues*; Sylvester, P., Ed.; Mineralogical Association of Canada Short Course 40: Vancouver, BC, Canada, 2008; pp. 328–333.
53. Szakáll, S.; Sajó, I.; Fehér, B.; Bigi, S. Ammoniomagnesiovoltaite, a voltaite-related mineral species from Pécs-Vasas, Hungary. *Can. Miner.* **2012**, *50*, 65–72. [[CrossRef](#)]
54. Deditius, A.P.; Utsunomiya, S.; Renock, D.; Ewing, R.C.; Ramana, C.V.; Becker, U.; Kesler, S.E. A proposed new type of arsenian pyrite: Composition, nanostructure and geological significance. *Geochim. Cosmochim. Acta* **2008**, *72*, 2919–2933. [[CrossRef](#)]
55. Deditius, A.P.; Reich, M. Constraints on the solid solubility of Hg, Tl, and Cd in arsenian pyrite. *Am. Miner.* **2016**, *101*, 1451–1459. [[CrossRef](#)]
56. George, L.L.; Biagioni, C.; D’Orazio, M.; Cook, N.J. Textural and trace element evolution of pyrite during greenschist facies metamorphic recrystallization in the southern Apuan Alps (Tuscany, Italy): Initiation of Tl-rich sulphosalt melt formation. *Ore Geol. Rev.* **2018**, *102*, 59–105. [[CrossRef](#)]
57. George, L.L.; Biagioni, C.; Lepore, G.O.; Lacalamita, M.; Agrosi, G.; Capitani, G.C.; Bonaccorsi, E.; d’Acapito, F. The speciation of thallium in (Tl, Sb, As)-rich pyrite. *Ore Geol. Rev.* **2019**, *107*, 364–380. [[CrossRef](#)]
58. Kolker, A. Minor element distribution in iron disulfides in coal: A geochemical review. *Int. J. Coal Geol.* **2012**, *94*, 32–43. [[CrossRef](#)]
59. Large, R.R.; Halpin, J.A.; Danyushevsky, L.V.; Maslennikov, V.V.; Bull, S.W.; Long, J.A.; Gregory, D.D.; Lounejeva, E.; Lyons, T.W.; Sack, P.J.; et al. Trace element content of sedimentary pyrite as a new proxy for deep-time ocean-atmosphere evolution. *Earth Planet. Sci. Lett.* **2014**, *389*, 209–220. [[CrossRef](#)]
60. Wells, J.D.; Mullens, T.E. Gold-bearing arsenian pyrite determined by microprobe analysis, Cortez and Carlin gold mines, Nevada. *Econ. Geol.* **1973**, *28*, 187–201. [[CrossRef](#)]
61. Deditius, A.P.; Utsunomiya, S.; Kesler, S.E.; Reich, M.; Ewing, R.C. Trace elements nanoparticles in pyrite. *Ore Geol. Rev.* **2011**, *42*, 32–46. [[CrossRef](#)]
62. Pearce, C.I.; Pattrick, R.A.D.; Vaughan, D.J. Electrical and magnetic properties of sulphides. *Rev. Miner. Geochem.* **2006**, *61*, 127–180. [[CrossRef](#)]
63. Klemm, D.D. Synthesen und analysen in den dreiecks diagrammen FeAsS-CoAsS-NiAsS und FeS<sub>2</sub>-CoS<sub>2</sub>-NiS<sub>2</sub>. *Neues Jahrbuch Fur Miner. Abh.* **1965**, *103*, 205–255. (In German)
64. Huston, D.L.; Sie, S.H.; Suter, G.F.; Cooke, D.R.; Both, R.A. Trace elements in sulfide minerals from Eastern Australian volcanic-hosted massive sulfide deposits: Part 1. Proton microprobe analyses of pyrite, chalcopyrite and sphalerite, and Part II. Selenium levels in pyrite: Comparison with  $\delta^{34}\text{S}$  values and implications for the source of sulfur in volcanogenic hydrothermal systems. *Econ. Geol.* **1995**, *90*, 1167–1196.
65. Zidarova, B.; Zidarov, N. Main elements of the local geogenetic model for fluorite formation: III. Chiprovci-East deposit. *C. R. Acad. Bulg. Sci.* **2000**, *53*, 63–66.
66. Dimitrova, D.; Kerestedjian, T.; Petrova, M. Cinnabar-pyrite mineralization associated with fluorite replacement bodies in the Chiprovtsi silver-lead deposit, Northwestern Bulgaria. In Proceedings of the 9th Biennial SGA Meeting Mineral Exploration and Research: Digging Deeper, Dublin, Ireland, 20–23 August 2007; pp. 873–876.

67. Nesbitt, H.W.; Scaini, M.; Hochst, H.; Bancroft, G.M.; Schaufuss, A.G.; Szargan, R. Synchrotron XPS evidence for Fe<sup>2+</sup>-S and Fe<sup>3+</sup>-S surface species on pyrite fracture surfaces, and their 3D electronic states. *Am. Miner.* **2000**, *85*, 850–857. [[CrossRef](#)]
68. Xiong, Y. Hydrothermal thallium mineralization up to 300 °C: A thermodynamic approach. *Ore Geol. Rev.* **2007**, *32*, 291–313. [[CrossRef](#)]
69. Hawthorne, F.C.; Krivovichev, S.V.; Burns, P.C. The crystal chemistry of sulfate minerals. *Rev. Miner. Geochem.* **2000**, *40*, 1–112. [[CrossRef](#)]
70. Bigham, J.M.; Nordstrom, D.K. Iron and aluminum hydroxysulfates from acid sulfate waters. *Rev. Miner. Geochem.* **2000**, *40*, 351–403. [[CrossRef](#)]
71. Kelly, D.P.; Wood, A.P. Reclassification of some species of Thiobacillus to the newly designated genera Acidithiobacillus gen. nov.; Halothiobacillus gen. nov. and Thermithiobacillus gen. nov. *Int. J. Syst. Evol. Microbiol.* **2000**, *50*, 511–516. [[CrossRef](#)]
72. Chukanov, N.V.; Aksenov, S.M.; Rastvetaeva, R.K.; Möhn, G.; Rusakov, V.S.; Pekov, I.V.; Scholz, R.; Eremina, T.A.; Belakovskiy, D.I.; Lorenz, J.A. Magnesiovoltaite, K<sub>2</sub>Mg<sub>5</sub>Fe<sup>3+</sup><sub>3</sub>Al(SO<sub>4</sub>)<sub>12</sub>·18H<sub>2</sub>O, a new mineral from the Alcaparossa mine, Antofagasta region, Chile. *Eur. J. Miner.* **2016**, *28*, 1005–1017. [[CrossRef](#)]
73. Majzlan, J.; Schlicht, H.; Wierzbicka-Wieczorek, M.; Giester, G.; Pöllmann, H.; Brömme, B.; Doyle, S.; Buth, G.; Koch, C.B. A contribution to the crystal chemistry of the voltaite group: Solid solutions, Mössbauer and infrared spectra, and anomalous anisotropy. *Miner. Petrol.* **2013**, *107*, 221–233. [[CrossRef](#)]
74. Jamieson, H.E.; Robinson, C.; Alpers, C.N.; Blaine McCleskey, R.; Nordstrom, D.K.; Peterson, R.C. Major and trace element composition of copiapite-group minerals and coexisting water from the Richmond mine, Iron Mountain, California. *Chem. Geol.* **2005**, *215*, 387–405. [[CrossRef](#)]
75. Majzlan, J.; Michalik, R. The crystal structures, solid solutions and infrared spectra of copiapite-group minerals. *Miner. Mag.* **2007**, *71*, 553–569. [[CrossRef](#)]
76. Shannon, R.D. Revised effective ionic radii and systematic studies of interatomic distances in halides and chalcogenides. *Acta Crystallogr.* **1976**, *A32*, 751–767. [[CrossRef](#)]
77. Majzlan, J.; Alpers, C.N.; Koch, C.B.; McCleskey, R.B. Vibrational, X-ray absorption, and Mössbauer spectra of sulfate minerals from the weathered massive sulfide deposit at Iron Mountain, California. *Chem. Geol.* **2011**, *284*, 296–305. [[CrossRef](#)]
78. Moncur, M.C.; Ptacek, C.J.; Blowes, D.W.; Peterson, R.C. The occurrence and implications of efflorescent sulfate minerals at the former Sherrit-Gordon Zn-Cu mine, Sherridon, Manitoba, Canada. *Can. Miner.* **2015**, *53*, 961–977. [[CrossRef](#)]
79. Romero, A.; González, I.; Galán, E. The role of efflorescent sulfates in the storage of trace elements in stream waters polluted by acid mine-drainage: The case of Peña del Hierro, Southwestern Spain. *Can. Miner.* **2006**, *44*, 1431–1446. [[CrossRef](#)]
80. Hammarstrom, J.M.; Seal, R.R., II; Meierb, A.L.; Kornfeld, J.M. Secondary sulfate minerals associated with acid drainage in the eastern US: Recycling of metals and acidity in surficial environments. *Chem. Geol.* **2005**, *215*, 407–431. [[CrossRef](#)]
81. Kruszewski, Ł. Supergene sulfate minerals from the burning coal mining dumps in the Upper Silesian Coal Basin, South Poland. *Int. J. Coal Geol.* **2013**, *105*, 91–109. [[CrossRef](#)]
82. Stamatakis, M.G.; Baltatzis, E.G.; Skounakis, S.B. Sulfate minerals from a mud volcano in the Katakolo area, western Peloponnesus, Greece. *Am. Miner.* **1987**, *72*, 839–841.
83. Dimitrova, D.; Velitchkova, N.; Mladenova, V.; Kotsev, T.; Antonov, D. Heavy metal and metalloid mobilization and rates of contamination of water, soil and bottom sediments in the Chiprovtsi mining district, Northwestern Bulgaria. *Geol. Balc.* **2016**, *45*, 47–63.

